

Quantum resonances and decoherence for δ -kicked atoms

Sandro Wimberger^{1,2,3}, Italo Guarneri^{2,3,4} and Shmuel Fishman⁵

¹Max-Planck-Institut für Physik komplexer Systeme, Nöthnitzer Str. 38, D-01187 Dresden

²Università degli Studi dell' Insubria, Via Valleggio 11, I-22100 Como

³Istituto Nazionale per la Fisica della Materia, Unità di Milano, Via Celoria, I-20133 Milano

⁴Istituto Nazionale di Fisica Nucleare, Sezione di Pavia, Via Bassi 6, I-27100 Pavia

⁵Physics Department, Technion, Haifa IL-32000

e-mail: saw@mpipks-dresden.mpg.de

Abstract. The quantum resonances occurring with δ -kicked atoms when the kicking period is an integer multiple of the half-Talbot time are analyzed in detail. Exact results about the momentum distribution at exact resonance are established, both in the case of totally coherent dynamics and in the case when decoherence is induced by Spontaneous Emission. A description of the dynamics when the kicking period is close to, but not exactly at resonance, is derived by means of a quasi-classical approximation where the detuning from exact resonance plays the role of the Planck constant. In this way scaling laws describing the shape of the resonant peaks are obtained. Such analytical results are supported by extensive numerical simulations, and explain some recent surprising experimental observations.

PACS numbers: 05.45.Mt, 03.65.Yz, 72.15.Rn, 42.50.Vk

1. Introduction.

The present work is devoted to a detailed theoretical analysis of some of the quantum resonances occurring in the δ -kicked rotor, motivated by laboratory results obtained with experimental realizations of that system.

1.1. Background.

The δ -kicked rotor is a paradigm model in quantum chaology, and its theoretical importance is connected with the long-time properties of its evolution. Among these are effects of purely quantum origin such as dynamical localization [1, 2, 3, 4, 5, 6, 7, 8] and the quantum resonances [9, 10]. Despite compelling numerical evidence, dynamical localization could not be mathematically proven until very recently[‡]. The origin and

[‡] A proof for the case of sufficiently small kicking strength has been announced by J. Bourgain and S. Jitomirskaya while the present paper was being prepared for publication.

the main dynamical and spectral features of the quantum resonances are instead well understood in general mathematical terms [9, 11, 10, 12]. They are observed when the kicking frequency is commensurate to the natural frequencies of the rotor and typically result in a quadratic growth of the energy asymptotically in time.

Although the δ -kicked rotor is an abstract theoretical model, it has found an experimental realization using tools of atom optics, by a technique pioneered by Raizen and coworkers [13]. In present-day experiments laser-cooled Cesium atoms are periodically driven with a standing electromagnetic wave. As the frequency of the wave is slightly detuned from an internal atomic transition, a net force on the centres of mass of the atoms arises, proportional to the square of the driving field [14, 15]. The standing wave is periodic in space, so the atoms are subject to a periodic potential. The latter is turned on and off periodically in time, resulting in a sequence of short pulses, or “kicks”. In such experiments, the kicked atoms behave as individual particles with negligible interaction due to collision etc. [16, 17], so a single-particle theory is applicable. The nonzero duration of the kicking pulses sets a bound on the momentum range wherein the ideal δ -kicked rotor model is applicable. At large momenta the driving becomes adiabatic, leading to trivial localization in momentum for the classical and the quantum version of the rotor [18, 17]. Important properties of the δ -kicked rotor have been experimentally reproduced: *e.g.*, the exponential localization in momentum [13, 19] (away from resonances). In addition the influence of noise and decoherence [20, 21, 22, 23], and the effect of gravity in the case when the kicking direction is vertical have been examined in experiments (with possible applications in atomic interferometry [24, 25, 26] and quantum measurement theory [27, 28, 29, 30]).

While dynamical localization is a robust phenomenon, the quantum resonances are rather sensitive instead, and the correspondence between theory and experiments is less appealing in their case. The following items represent incomplete or missing matches between the δ -kicked rotor theory and experimental results [31, 32, 33]:

(i) quantum resonances occur for the δ -kicked rotor whenever the kicking period τ (in appropriate units) is a rational multiple of 4π , which is the Talbot time in the language of diffraction optics [32, 34, 35]. In experiments, only at the values $\tau = 2\pi, 4\pi, 6\pi$, a special behaviour has been observed, in the form of narrow peaks in the energy absorption vs. τ . This means that higher order resonances have not been resolvable within the experimental bounds.

(ii) *no quadratic* energy growth at resonance has been experimentally observed. “Ballistic peaks” were reported by Raizen *et al.* [31], due to a tiny fraction of atoms which indeed show a quadratically increasing energy. This is in contrast to the bulk of the atomic cloud, which is instead frozen in a rather narrow distribution in momentum. The latter is, however, not exponential, at variance with the distribution found at non-resonant values of τ , i.e. in the localized regime.

(iii) *an enhancement* of the resonant peaks has been experimentally observed with *increasing* degree of decoherence. This is especially surprising, because decoherence is expected to drive the quantum system towards a more classical behaviour, hence to

inhibit purely quantum effects, such as the quantum resonances of the δ -kicked rotor. As to dynamical localization, its destruction due to decoherence was experimentally observed in [36, 20, 21]§.

The listed findings do not match with the theory of the δ -kicked rotor, and various physical reasons have been identified. The simplest, yet deepest of these is the starting point of the present paper: the experiments do not provide a realization of the δ -kicked rotor but of the δ -kicked particle instead, the difference being that while rotors move in circles, particles move in (approximately) straight lines. This difference is irrelevant on the classical level, however it has nontrivial quantum implications, that lie within the scope of the Bloch theory. The quantum dynamical localization is not impaired (localization lengths and fluctuation properties are affected, though) [10]. Not so in what concerns the quantum resonances, that make the subject of this work.

1.2. Outline, and statement of results.

In this paper we analyze in mathematical detail the dynamics of atoms at quantum resonance and in its vicinity for the ideal case of δ -kicks. Our basic tool is the Bloch theory for quantum particles in periodic potentials. The basic constructions of that theory as applied to δ -kicked particles are shortly reviewed in section 2. Our main results are:

- (i) In the absence of decoherence, we show that the mean energy increases linearly with time (section 3.2.3) yet the motion is dynamically localized, in the sense that the momentum distribution settles in the course of time to a relatively narrow steady state distribution (section 3.2.2). This seeming contradiction is resolved by the slow algebraic decay of the tails of the steady state distribution. We give an integral expression (eq. (20),(18),(17)) of the latter distribution, whence we derive exact bounds (21) and large-momentum asymptotics (22).
- (ii) We derive a scaling law (section 4) that describes the shape of the resonant peaks which are observed in the energy vs. kicking period curves. The scaling law (36) is then demonstrated by numerical simulations. It is derived by means of a quasi-classical approximation (subsection 4.1), where the role of the Planck constant is played by the detuning from exact resonance. This technique was introduced in [25, 26]. It allows to describe the near-to-resonant quantum motion in terms of a Standard Map, which is different in parameter values from the one that is obtained in the usual classical limit of the δ -kicked rotor. The *quantum* resonance exactly corresponds to the main *classical* resonance of this standard map. The stable island associated with the latter resonance accounts for the structure of the resonant peaks. This analysis closely links quantum resonances with classical nonlinear ones, thus closing a gap between different meanings of the term “resonance”, which were deemed to be unrelated.

§ Similarly noise due to Spontaneous Emission affects non-dispersive quantum wave packets formed in highly excited Rydberg atoms [37, 38].

- (iii) We devise a model of stochastic δ -kicked rotor dynamics, where the external noise is modelled after the Spontaneous Emission (SE) effects that are used to induce controlled decoherence in experiments (section 5). Our statistical assumptions (subsection 5.2) are a compromise between physical adherence and mathematical convenience, and allow to derive simple exact results, that expose the key mechanism whereby the quantum resonances are affected. We explicitly compute the growth of the mean energy in time (eq. (64)). We prove that no steady state momentum distribution is any more attained, and that, in contrast, the momentum distribution evolves into a Gaussian distribution which spreads diffusively (subsection 5.2.4). By checking such results against realistic numerical simulations we demonstrate that their validity does not crucially depend on our technical assumptions (subsection 5.2.5). So they are relevant for a wide range of experimental situations.
- (iv) The stochastic δ -kicked rotor dynamics provides a remarkable example where the classical and quantum effects of the coupling to the environment can be separated. This is achieved by a stochastic gauge transformation (section 5.1).
- (v) We provide a description of the nearly resonant dynamics in the presence of decoherence (section 5.3), by means of the small-detuning quasi-classical asymptotics (point (ii) above). In this way we derive a scaling law for the structure of the resonant peaks in the presence of decoherence (eq. (79)), which is then demonstrated by numerical simulations.
- (vi) We explain the experimentally observed enhancement of the resonant peaks in the presence of SE (section 6). At a low degree of decoherence, the linear growth of energy at resonance (eq. (64)) is but slightly changed with respect to the decoherence-free case, so decoherence cannot by itself explain the much stronger enhancement of the resonant peaks that was experimentally observed. In order to understand the latter we analyse differences which experiments inevitably impose with respect to the ideal models. Experimental cutoffs in momentum exist, due on one hand to the finite duration of the pulses and on the other hand to the signal-to-noise ratio. Using the results of point (i) we argue, and numerically demonstrate, that the latter type of cutoff is responsible for the observed enhancement. The coherent energy growth at resonance is due only to the fastest atoms, hence it is stopped as soon as such atoms escape the finite bounds of experimental observation. This peculiarity is rapidly destroyed by decoherence, which calls for all the atoms to participate in the mean energy growth.

2. Kicked atoms vs. Kicked Rotors.

We consider a one-dimensional model for a kicked atom of mass M , subject to time- and space-periodic kicks, with periods T and πk_L^{-1} , respectively. k_L is the wave number of the kicking field whose maximum strength is given by κ . We rescale momentum in units of $2\hbar k_L$, position in units of $(2k_L)^{-1}$, mass in units of M . Energy is then given in units

of $\hbar^2(2k_L)^2/M$, time in units of $M/\hbar(2k_L)^2$, and the reduced Planck's constant equals 1. The dynamics of the kicked atoms is induced by the following Hamiltonian [26, 25], which depends on the continuous time parameter t' :

$$\hat{H}(t') = \frac{\hat{P}^2}{2} + k \cos(\hat{X}) \sum_{t=-\infty}^{+\infty} \delta(t' - t\tau), \quad (1)$$

where \hat{X}, \hat{P} are the position and the momentum operator respectively, $k = \kappa/\hbar$, and the kicking period $\tau = \hbar T(2k_L)^2/M$. The state evolution of the atom from one kick to immediately after the next kick is determined by the unitary Floquet operator:

$$\hat{U} = e^{-ik \cos(\hat{X})} e^{-i\tau \hat{P}^2/2}. \quad (2)$$

Iterated application of the one-cycle operator \hat{U} yields the dynamics of the atom in the discrete time given by the kick counter, which we denote by the *integer* t . We further denote $|\psi\rangle$ the state vector of the atom, and $\psi(x) = \langle x|\psi\rangle$, $\tilde{\psi}(p) = \langle p|\psi\rangle$ the wave functions in the position and in the momentum representation, respectively.

The model (2) differs from the kicked-rotor model because the particle does not move on a circle but on a line instead. A link between the two models is generated by the spatial periodicity of the kicking potential: the Floquet operator (2) commutes with spatial translations by multiples of 2π . As is well-known from the Bloch theory, this enforces conservation of the Quasi-Momentum (QM). In our units, QM is given by the fractional part $\{p\}$ of the momentum p and will be denoted β , ($0 \leq \beta < 1$). For a sharply defined value of quasi-momentum, the wave function of the atom is a Bloch wave, of the form $\exp(i\beta x)\psi_\beta(x)$, with $\psi_\beta(x)$ a 2π -periodic function. The general particle wave packet is obtained by superposing Bloch waves parametrized by the continuous variable $\beta \in [0, 1)$:

$$\psi(x) = \int_0^1 d\beta e^{i\beta x} \psi_\beta(x). \quad (3)$$

Denoting $\theta \equiv x \bmod(2\pi)$, we in turn have

$$\psi_\beta(\theta) = \frac{1}{\sqrt{2\pi}} \sum_n \tilde{\psi}(n + \beta) e^{in\theta}. \quad (4)$$

In the special case when the state of the particle is a plane wave with momentum p_0 , then

$$\psi_\beta(\theta) = (\sqrt{2\pi})^{-1} \delta(\beta - \beta_0) \exp(in_0\theta), \quad (5)$$

where $\beta_0 = \{p_0\}$ and $n_0 = [p_0]$ are the fractional and integer part of p_0 , respectively.

For any given β , $\psi_\beta(\theta)$ may be thought of as the wave function of a rotor with angular coordinate θ , henceforth called β -rotor. We denote the corresponding state of the rotor by $|\psi_\beta\rangle$. From (2) and (4), it follows that, while $|\psi\rangle$ evolves into $\hat{U}|\psi\rangle$, $|\psi_\beta\rangle$ evolves into $\hat{U}_\beta|\psi_\beta\rangle$, with

$$\hat{U}_\beta = e^{-ik \cos(\hat{\theta})} e^{-i\frac{\tau}{2}(\hat{N} + \beta)^2}, \quad (6)$$

where \hat{N} is the angular momentum operator: in the θ -representation, $\hat{N} = -id/d\theta$ with periodic boundary conditions. The Floquet operator (6) differs from the Floquet operator of the standard δ -kicked rotor by the phase β . In previous studies of this rotor variant, β was typically regarded as an external Aharonov-Bohm flux [39].

3. Quantum resonances.

The time evolution determined by the Floquet operator (6) preserves many of the dynamical properties of the standard δ -kicked rotor (corresponding to $\beta = 0$), but not necessarily the quantum resonances. These only occur for special values of quasi-momentum [10]. Whenever $\tau = 4\pi p/q$ (p, q mutually prime integers), and $\beta = m/2p$ with m an integer such that $0 \leq m < 2p$, the operator (6) commutes with translations in momentum space by multiples of q , leading to bands in its quasi-energy spectrum. For special values of q , the bands may be flat, i.e., of zero width; such is the case, e.g., for $q = 2$, m an even integer. In typical cases, however, the bands are not flat and result in absolutely continuous quasi-energy spectra, that enforce ballistic growth of momentum. The width of the bands rapidly decreases as the order q of the resonance increases [9,10], so ballistic motion is observable only after quite long times. This makes higher-order resonances experimentally hardly detectable, and provides an already well-known answer to the first problem (i) stated in the Introduction (subsection 1.1). Further reasons hindering experimental observation of higher resonances are pointed out in section 6.

3.1. β -rotor dynamics.

We focus on the main resonances $q = 1, 2$ in the following, i.e., we set $\tau = 2\pi\ell$, with ℓ a positive integer. Inserting this value for the kicking period into (6), and using the identity $\exp(-i\pi n^2\ell) = \exp(-i\pi n\ell)$, we obtain (apart from an n -independent phase factor)

$$\hat{\mathcal{U}}_\beta = e^{-ik \cos(\hat{\theta})} e^{-i\xi \hat{\mathcal{N}}} \quad (7)$$

where $\xi \equiv \pi\ell(2\beta \pm 1) \bmod(2\pi)$ will be taken in $[-\pi, \pi)$. The 2nd operator on the rhs of (7) will be denoted $\hat{\mathcal{R}}(\xi)$. In the θ -representation it acts according to:

$$(\hat{\mathcal{R}}(\xi)\psi_\beta)(\theta) = \psi_\beta(\theta - \xi) . \quad (8)$$

The state after the t -th kick is then given by

$$(\hat{\mathcal{U}}_\beta^t \psi_\beta)(\theta) = e^{-ikF(\theta, \xi, t)} \psi_\beta(\theta - t\xi) , \quad (9)$$

with

$$F(\theta, \xi, t) = \sum_{s=0}^{t-1} \cos(\theta - s\xi) = |W_t| \cos(\theta + \arg(W_t)) , \quad (10)$$

where $W_t = W_t(\xi) := \sum_{s=0}^{t-1} e^{-is\xi}$. We denote by n the eigenvalues of the angular momentum $\hat{\mathcal{N}}$. Then, in the $\hat{\mathcal{N}}$ representation, the state (9) reads (after changing variable from θ to $\theta + \arg(W_t)$):

$$\langle n | \hat{\mathcal{U}}_\beta^t \psi_\beta \rangle = e^{in \arg(W_t)} \int_0^{2\pi} \frac{d\theta}{\sqrt{2\pi}} e^{-in\theta - ik|W_t| \cos(\theta)} \psi_\beta(\theta - t\xi - \arg(W_t)) . \quad (11)$$

If the initial state of the particle is a plane wave (5) of momentum $p_0 = n_0 + \beta_0$, then ξ takes the constant value $\xi_0 = \pi\ell(2\beta_0 - 1)$. Substituting in (11), and computing the

integral by means of formula (E.1), the momentum distribution for the β_0 -rotor at time t is:

$$P(n, t|n_0, \beta_0) = J_{n-n_0}^2(k|W_t|), \quad (12)$$

where $J_n(\cdot)$ is the Bessel function of first kind and order n . Using the Bessel function identity (E.2), one computes the expectation value of p^2 (or the energy by dividing by 2):

$$\overline{p^2}(n_0, \beta_0, t) = \sum_n (n + \beta_0)^2 P(n, t|n_0, \beta_0) = (n_0 + \beta_0)^2 + \frac{1}{2}k^2|W_t|^2. \quad (13)$$

Explicit computation of (10) yields:

$$|W_t| = \left| \frac{\sin(t\xi_0/2)}{\sin(\xi_0/2)} \right| \text{ if } \xi_0 \neq 0. \quad (14)$$

If $\xi_0 = 0$ then $|W_t| = t$. Then the distribution (12) spreads linearly in time, and the average kinetic energy increases like $k^2 t^2/4$. The corresponding spread over the discrete momentum ladder is the same as for a free particle under the time evolution generated by the discrete Laplacian operator. $\xi_0 = 0$ corresponds to $\beta_0 = 1/2 + n/\ell \text{ mod}(1)$, $n = 0, 1, \dots, \ell - 1$, the resonant values of β which were mentioned in the beginning of the present Section. For any other value of β , the distribution changes in time in a quasi-periodic manner. It oscillates in time with the approximate period $\pi\xi_0^{-1}$, inverse to the detuning of β_0 from the nearest resonant value. At any time t , it is negligible at $|n - n_0| > k|\text{csc}(\xi_0/2)|$.

3.2. Incoherent ensemble of atoms.

If the initial state of the particle is a wave packet, then it is a coherent superposition of continuously many plane waves with different quasi-momenta, which are non-resonant except for a finite set of values. It can then be proven that the asymptotic growth of energy in time is proportional to $k^2 t/4$ [26]. Here we consider the case when the initial atomic ensemble is an incoherent mixture of plane waves. Numerical simulations based on such choices of an initial state have shown satisfactory agreement with experimental data [40, 33]. The initial momentum distribution shall be described by a density $f(p)$. We can equivalently consider an ensemble of β -rotors with β distributed in $[0, 1]$ with the density:

$$f_0(\beta) = \sum_{n=-\infty}^{+\infty} f(n + \beta). \quad (15)$$

In the case when $f(p)$ is Gaussian with standard deviation σ (a reasonable assumption for the Oxford experiments according to [31, 33]), $f_0(\beta)$ is a Theta-function, and Poisson's summation formula yields:

$$f_0(\beta) = 1 + 2e^{-2\pi^2\sigma^2} \cos(2\pi\beta) + O(e^{-8\pi^2\sigma^2}). \quad (16)$$

For $\sigma > 1$, that is relevant for the present day experiments, it is practically indistinguishable from the uniform distribution $f_0(\beta) = 1$. Each β -rotor is described

by a statistical state, which attaches the probability $f_0(\beta)^{-1}f(n + \beta)$ to the momentum eigenstate $|n\rangle$. The momentum distribution $P(p, t)$ of the particle at time t is obtained as follows. For any given $\beta_0 \in [0, 1)$, averaging (12) over the different n_0 of the initial distribution yields the momentum distribution $\bar{P}(n, t|\beta_0)$ for the β_0 -rotor. Weighted by $f_0(\beta_0)$, this is the same as the momentum distribution $P(p, t)$ of the particle over the ladder $p = n + \beta_0$ (β_0 fixed, n variable). The on-ladder distributions corresponding to different β_0 combine like a jig-saw puzzle in building the global momentum distribution for the particle. The result is a complicated function of p that oscillates on the scale $1/t$ (see the ξ_0 -dependence of (12),(14)). Nevertheless, in the average, this distribution evolves into a steady state distribution. This may be shown either by time-averaging, or by coarse-graining, as done in the following subsections.

3.2.1. Time-averaged distribution. As $t \rightarrow \infty$, the time average of the distribution (12) tends to 0 whenever β_0 has a resonant value, because the ballistic flight of atoms with a resonant quasi-momentum results in vanishing probability of being found in any *finite* momentum interval. For any non-resonant value of β_0 , the distribution (12) tends in time-average to a distribution $P^*(n|n_0, \beta_0)$. In fact, for non-resonant β_0 the time average of (12) is just the average of $J_{n-n_0}^2(k \sin(\alpha) \csc(\xi/2))$ along the trajectory of the shift $\alpha \rightarrow \alpha + \xi_0/2(\text{mod}2\pi)$, starting from $\alpha = 0$. If β_0 is a non-resonant rational, then the trajectory is periodic and the time average trivially converges. If β_0 is irrational, the shift is ergodic, so the time average converges to the phase average. The time-averaged momentum distribution for the β_0 -rotor is thus given, for irrational β_0 , by the following integral expression:

$$P^*(n|n_0, \beta_0) = \frac{1}{2\pi} \int_0^{2\pi} d\alpha J_{n-n_0}^2(k \sin(\alpha) \csc(\pi\ell(\beta_0 - \frac{1}{2}))). \quad (17)$$

It follows that the momentum distribution $P(p, t)$ for the atom converges, in time average, to a steady-state distribution $P^*(p)$. This is obtained by averaging over n_0 the time-averaged distribution $P^*(n|n_0, \beta_0)$ discussed above for the β -rotors, and by combining the on-ladder distributions $P^*(n|\beta_0)$ thus obtained. Note that the **rhs** of (17), albeit a continuous function of β_0 , does not necessarily coincide with the lhs when β_0 is rational. Hence $P^*(p)$ has, strictly speaking, a dense set of discontinuities formed by values of p with a rational non-resonant fractional part β . Nevertheless (17) is adequate for computing averages of smooth functions of p . A time-averaged distribution (17) is shown in Fig. 1 for $\ell = 1$ and for the case of an initially flat momentum distribution in $[0, 1)$. In this case $n_0 = 0$, and the integral (17) was numerically computed for each n, β_0 . The distribution is not seen to vanish at $n + 1/2$ because the computational grid in p was chosen at random, thus avoiding simple rational numbers. Discontinuities at integer p are clearly visible. They are due to the discontinuity of the initial momentum (box) distribution at $p = 0, 1$, and are not related to the above discussed ones. In the momentum intervals $n < p < n + 1$ with $n \gg k$ the distribution $P^*(p)$ is negligibly small except in a neighbourhood of width $2/n$ around $n + 1/2$. This is due to the faster-than-exponential decay of the Bessel functions when their order increases beyond

the argument. At $p = n + 1/2$ the distribution is exactly zero. Thus in all intervals $n < p < n + 1$, $P^*(p)$ has the form of two narrow peaks, situated symmetrically wrt $n + 1/2$. As shown in the next subsection, the total probability in such intervals decays like $1/n^2$, so the height of the twin peaks decays like $1/n$, as is indeed clear from Fig. 1. Cases with $\ell > 1$ may be discussed along similar though not identical lines.

3.2.2. Coarse-grained distribution. The second way of removing the fast oscillations is replacing $P(p, t)$ in each interval $n < p < n + 1$ by its integral $P_n(t)$ over that interval. This corresponds to using a bin size $2\hbar k_L$ for the observed distributions. Assuming $f(p)$ to be coarse-grained itself, the new distribution is approximately computed in the form:

$$P_n(t) = \sum_m M_{n-m}(t) f(m), \quad (18)$$

where

$$\begin{aligned} M_n(t) &= \int_0^1 d\beta J_n^2(k|W_t|) = \int_{-\pi}^{\pi} \frac{dx}{2\pi} J_n^2(k \sin(tx) \csc(x)) \\ &= \int_{-\pi}^{\pi} \frac{dx}{4\pi^2} \sum_{r=0}^{t-1} \frac{2\pi}{t} J_n^2(k \sin(x) \csc(xt^{-1} + 2\pi r t^{-1})). \end{aligned} \quad (19)$$

In the limit when $t \rightarrow \infty$ and $2\pi r/t \rightarrow \alpha$, the sum over r approximates the integral over α , and (19) converges to

$$M_n^* = (2\pi)^{-2} \int_{-\pi}^{\pi} dx \int_0^{2\pi} d\alpha J_n^2(k \sin(x) \csc(\alpha)). \quad (20)$$

The steady-state coarse-grained distribution P_n^* is then obtained by replacing (20) in (18). Note that it is the coarse-grained distribution itself, and not just its time-average, that converges to the steady-state distribution. We do not know if the double integral may be computed in closed form. In Appendix A we prove the following (non-optimal) estimate, valid for $N > k$:

$$\sum_{|n| \geq N} M_n^* \leq 2 \left(\frac{ke}{16} \right)^{\frac{2N}{2N+1}} N^{\frac{1-2N}{1+2N}} \left(2 + \frac{1}{N} \right). \quad (21)$$

Using this estimate it is easy to compute that for $k > 1$ the total probability carried by states $|n| > 4k$ is not larger than $0.31 \dots$; so, at large k , the distribution is rather narrow as compared to the exponentially localized distribution which is observed far from resonance, because the width of the latter scales like k^2 . In Appendix A we further prove that the distribution (20) has the following large- $|n|$ asymptotics:

$$M_n^* \sim \frac{4k}{\pi^3 n^2} \text{ as } |n| \rightarrow \infty. \quad (22)$$

Such a decay carries over to the coarse-grained distribution P_n^* whenever $f(p)$ is fast decaying (e.g., like a Gaussian).

The convergence of the coarse-grained distributions to the steady-state distribution is illustrated in Fig. 2, that were produced by numerically simulating the evolution

of statistical ensembles of particles, with an initial Gaussian momentum distribution. The central part of the distribution quite early stabilizes in the final form of a narrow peak of width $\sim k$. Away from this peak, the algebraic tail $\propto n^{-2}$ develops over larger and larger momentum ranges as time increases in the wake of two symmetric, tiny “ballistic peaks”^{||}, that move away linearly in time. The fall of the distribution is quite steep past such peaks. This is easily understood from the first equation in (19): since $|\sin(tx) \csc(x)| \leq \pi t/2$, at $n > \pi kt/2$ the integrand decays faster than exponentially. The distribution in Fig. 2 (b) has stabilized to the limit distribution over a broad momentum range. Apart from the far tail, where the moving peak structure is still apparent, the distribution follows the asymptotic decay (22) already for $|n| \gtrsim 15$. Hence, using (22), the total probability on states $|n| > 40$ is $\sim 8 \times 10^{-3}$.

From the above analysis, we obtain that all moments of p of order ≥ 1 diverge as $t \rightarrow \infty$, in spite of the onset of the stationary distribution, due to the slow algebraic decay of the latter. For the case of the 2nd moment, which is (apart from a factor 2) just the mean energy of the ensemble, the growth is actually *linear in time*, as we shall presently show.

3.2.3. Average kinetic energy. The mean kinetic energy of an ensemble of rotors at time t is obtained by averaging (13) over the initial momentum distribution:

$$\mathcal{E}\{\bar{E}(t)\} = \mathcal{E}\{\bar{E}(0)\} + \frac{k^2}{4} \int_0^1 d\beta f_0(\beta) \frac{\sin^2(t\pi\ell(\beta - 1/2))}{\sin^2(\pi\ell(\beta - 1/2))}. \quad (23)$$

As $t \rightarrow \infty$, the fraction in the integrand, multiplied by ℓ/t , tends to a periodic δ function of $(\beta - 1/2)$ with period $1/\ell$. Thus (23) has the following $t \rightarrow \infty$ asymptotics:

$$\mathcal{E}\{\bar{E}(t)\} \sim \mathcal{E}\{\bar{E}(0)\} + \frac{k^2 t}{4\ell} \sum_{j=0}^{\ell-1} f_0(\beta^{(j)}). \quad (24)$$

where $\beta^{(j)} = 1/2 + j/\ell \bmod(1)$ are the resonant quasi-momenta. In the case when $f_0(\beta) \equiv 1$, i.e., it is uniform in $[0, 1)$, this formula is exact for *all* times t (by (E.7)). It is practically exact at all times for an initial Gaussian distribution with width $\sigma > 1$ around the origin; for, indeed, $f_0(\beta)$ is nearly uniform in that case, as noted in section 3.2. Higher order energy moments may be likewise computed. For large, finite t the n^{-2} decay of the distribution is truncated at $n \sim kt$ and is thereafter replaced by a much faster decay. Consequently, the variance of energy increases like t^3 . The increase of other moments may also be estimated in this way.

4. Dynamics near to Resonance.

The experimental observation of quantum resonances is mainly based on measuring the average energy of the kicked atoms after a fixed time t_{obs} . For all sufficiently

^{||} This denotation is borrowed from [31], where experimental observation of such structures was reported.

irrational values of the kicking period τ , the theory of the ideal kicked rotor model predicts localization, that is, on increasing t_{obs} beyond a *break-time* t^* , the observed energy values should not increase any more. In contrast, resonant values of τ lead to unbounded growth of energy[¶] with t_{obs} , as analyzed in previous sections for the particular cases $\tau = 2\pi\ell$. Hence, if t_{obs} is significantly larger than t^* , then a scan of the measured energy versus the kicking period τ yields plots similar to the (numerically obtained) one shown in Fig. 3(a), where peaks are clearly observed at the resonant values $\tau = 2\pi\ell$. For obvious continuity reasons, such peaks have a width, determined by the finite value of t_{obs} . In the ideal case, they would shrink on increasing t_{obs} , and further, narrower peaks associated with higher-order resonances would appear. In this section we derive a description of the structure of the peaks around $\tau = 2\pi\ell$, based on a finite time, small- ϵ asymptotics, where $\tau = 2\pi\ell + \epsilon$. This technique was introduced in [25,26]. We in particular find that the width of the resonant peak scales like $(kt_{obs}^2)^{-1}$, so that at large t_{obs} the peak is much narrower than the naive expectation $\propto 1/t_{obs}$.

4.1. ϵ -quasi classical asymptotics near resonance.

We rescale $k = \tilde{k}/|\epsilon|$, and define

$$\hat{I} = |\epsilon|\hat{\mathcal{N}} = -i|\epsilon|\frac{d}{d\theta}, \quad \hat{\mathcal{H}}_\beta(\hat{I}, t) = \frac{1}{2}\text{sign}(\epsilon)\hat{I}^2 + \hat{I}(\pi\ell + \tau\beta). \quad (25)$$

Then the Floquet operator for the β -rotor may be rewritten in the form:

$$\hat{\mathcal{U}}_\beta(t) = e^{-\frac{i}{|\epsilon|}\tilde{k}\cos(\hat{\theta})} e^{-\frac{i}{|\epsilon|}\hat{\mathcal{H}}_\beta}. \quad (26)$$

If $|\epsilon|$ is regarded as the Planck's constant, then (25),(26) is the formal quantization of either of the following classical maps:

$$I_{t+1} = I_t + \tilde{k}\sin(\theta_{t+1}), \quad \theta_{t+1} = \theta_t \pm I_t + \pi\ell + \tau\beta \pmod{2\pi} \quad (27)$$

where \pm has to be chosen according to the sign of ϵ . We stress that ‘‘classical’’ here is not related to the $\hbar \rightarrow 0$ limit but to the limit $\epsilon \rightarrow 0$ instead. The small- $|\epsilon|$ asymptotics of the quantum β -rotor is thus equivalent to a quasi-classical approximation based on the ‘‘classical’’ dynamics (27), that will be termed ϵ -classical in the following. Changing variables to $J = \pm I + \pi\ell + \tau\beta$, $\vartheta = \theta + \pi(1 - \text{sgn}(\epsilon))/2$ turns the maps (27) into a single Standard Map, independent of the value of β :

$$J_{t+1} = J_t + \tilde{k}\sin(\vartheta_{t+1}), \quad \vartheta_{t+1} = \vartheta_t + J_t. \quad (28)$$

This will be called the ϵ -classical Standard Map (ϵ SM) in what follows. In Fig. 4 quantum energy curves vs. τ in a neighbourhood of $\tau = 2\pi$ are compared with energy curves computed using the ϵ -classical map (27). For any given particle in the initial ensemble, the map (27) with β equal to the quasi-momentum of the particle was used to compute a set of trajectories started at $I = n_0|\epsilon|$ with homogeneously distributed $\theta \in [0, 2\pi)$. The final energies $\epsilon^{-2}I_t^2/2$ at $t = t_{obs}$ of the individual trajectories were

[¶] Unbounded growth was also proven for a dense set of close-to-commensurate values of τ [11]. Extremely long times are however required to resolve such arithmetic subtleties.

averaged over θ, β, n_0 with the appropriate weights. This is equivalent to using the ϵ SM in all cases, with different initial ensembles $J_0 = \text{const} = \pm n_0 |\epsilon| + \pi \ell + \tau \beta_0$. As β_0 is varied, such ensembles sweep the full unit cell of the ϵ SM, so sampling different β_0 's amounts to probing different regions of the ϵ -classical phase space. The average energy $\langle E_t \rangle = \epsilon^{-2} \langle I_t^2 \rangle / 2$ is plotted vs. $\tau = 2\pi + \epsilon$ in Fig. 4, along with results of the corresponding quantal computations. The main qualitative features emerging of Fig. 4 are: (i) On a gross scale the curves are shaped in the form of a basin with a high, narrow spike in the centre, closely flanked by a much smaller peak on either side. (ii) Quantum and ϵ -classical curves nicely agree at small $|\epsilon|$, in particular the structure of the spike is the same. Their behaviour at large $|\epsilon|$ is qualitatively similar but quantitatively different.

This overall qualitative behaviour may be explained in ϵ -classical terms, and an approximate scaling law for the t, k, ϵ dependence of the mean energy close to resonance may be obtained, as shown in the next section.

4.1.1. ϵ -quasi-classical analysis of the resonant peaks. The ϵ -classical standard map is different from the map obtained in the classical limit proper $\hbar \rightarrow 0$ of the kicked rotor. In particular, if $2\pi \ell k > 1$, then the classical and the ϵ -classical dynamics are at sharp variance whenever $\tilde{k} < 1$. In the former unbounded diffusion occurs; in the latter the dynamics is quasi-integrable instead, and the ϵ -classical trajectories remain trapped forever in-between KAM curves. It is exactly the deep changes which occur in the ϵ -classical phase space as τ is varied at constant k that account for the energy vs. τ dependence at fixed time $t = t_{obs}$. In the following discussion we assume for simplicity an initially flat distribution of $p \in [0, 1]$; then $I_0 = 0$, and $J_0 = \pi \ell + \tau \beta_0$ with β_0 uniformly distributed in $[0, 1)$. Without loss of generality we also consider $\ell = 1$. Hence if $|\epsilon| \ll 1$ then J_0 is uniformly distributed over one period (in action) $(\pi, 3\pi)$ of the ϵ SM.

Since $J_t = \pm I_t + \pi + \tau \beta$, and $I_0 = 0$, the mean energy of the rotor at time t is:

$$\langle E_{t,\epsilon} \rangle = \epsilon^{-2} \langle I_t^2 \rangle / 2 = \epsilon^{-2} \langle (\delta J_t)^2 \rangle / 2, \quad \delta J_t = J_t - J_0.$$

The exact quantum resonance $\epsilon = 0$ corresponds to the integrable limit of the ϵ SM, where $\delta J_t = 0$. However, $\langle E_{t,\epsilon} \rangle$ is scaled by ϵ^{-2} , so in order to compute it at $\epsilon = 0$ one has to compute δJ_t at first order in ϵ . This is done by substituting the 0-th ϵ -order of the 2nd equation into the 1st equation of (28). This leads to:

$$\delta J_t = |\epsilon| k \sum_{s=0}^{t-1} \sin(\theta_0 + J_0 s) + r(\epsilon, t) \quad (29)$$

where $r(\epsilon, t) = o(\epsilon)$ as $\epsilon \rightarrow 0$ at any fixed t . The energy at time t is found from (29) by taking squares, averaging over θ_0, J_0 , dividing by $2|\epsilon|^2$, and finally letting $\epsilon \rightarrow 0$. With the help of (E.7), this calculation yields:

$$\langle E_{t,0} \rangle = \frac{k^2}{8\pi} \int_{\pi}^{3\pi} dJ_0 \frac{\sin^2(J_0 t / 2)}{\sin^2(J_0 / 2)} = \frac{k^2}{4} t. \quad (30)$$

The small contribution of the initial quasi-momentum in the atom's energy was neglected. Apart from that, (30) is the same result as was found by the exact quantum mechanical calculation performed at $\epsilon = 0$ and $\ell = 1$ in section 3.2.3 for the case of a uniform QM distribution, see (23). Thus the ϵ -quasi-classical approximation reproduces the quantum behaviour at exact quantum resonance.

The integral over J_0 in (30) collects contributions from all the invariant curves $J_0 = \text{const.}$ of the ϵ SM at $\epsilon = 0$. Of these, the one at $J_0 = 2\pi$ leads to quadratic energy growth because it consists of (period 1) fixed points. This is called a classical resonance. It is responsible for the linear growth of energy (30), because the main contribution to the integral in (30) comes from a small interval $\sim 2\pi/t$ of actions around $J_0 = 2\pi$. Note that $J_0 = 2\pi$ corresponds to $\beta_0 = 1/2$, the “resonant” value of quasi-momentum. It is hence seen that the ϵ -quasi-classical approximation explains the *quantum* resonances of the KR in terms of the *classical* resonances of the Standard Map.

We shall now estimate $\langle E_{t,\epsilon} \rangle$ for $|\epsilon| > 0$. The $|\epsilon| > 0$ dynamics is maximally distorted with respect to the $\epsilon = 0$ one for J_0 in the vicinity of $2n\pi$, that is, in the very region which is mostly responsible for the linear growth of energy at $\epsilon = 0$. Being formed of period-1 fixed points, the $J_0 = 2n\pi$, $\epsilon = 0$ invariant curves break at $|\epsilon| > 0$ as described by the Poincaré-Birkhoff theorem [41]. The motion is then strongly distorted inside regions of size (in action) δJ_{res} astride $J = 2n\pi$. Such regions are termed the “main resonances” of the ϵ SM, and a well known estimate has $\delta J_{res} \approx 4(k|\epsilon|)^{1/2}$ [41]. Inside such regions, the approximation (29) fails quite quickly, so their contribution $\langle E_t \rangle_{res}$ in the mean energy has to be differently estimated.

In the remaining part of the ϵ -classical phase space the motion mostly follows KAM invariant curves, slightly deformed with respect to the $\epsilon = 0$ ones, still with the same rotation angles. The contribution $\langle E_t \rangle_{KAM}$ of such invariant curves in the mean energy is therefore roughly similar to that considered in the integral (30), provided J_0 is therein meant as the rotation angle⁺. On such grounds, in order to roughly estimate $\langle E_{t,\epsilon} \rangle$ we remove from the integral (30) the contribution of the resonant action interval near $J_0 = 2\pi$, and we replace it by $\langle E_t \rangle_{res}$:

$$\langle E_{t,\epsilon} \rangle \sim \frac{k^2}{4}t - \Phi(t) + \langle E_t \rangle_{res}, \quad (31)$$

where

$$\Phi(t) = \frac{k^2}{8\pi} \int_{-\delta J_{res}/2}^{\delta J_{res}/2} dJ' \frac{\sin^2(tJ'/2)}{\sin^2(J'/2)}, \quad (32)$$

and J' is the deviation from the resonant value 2π . The contribution $\langle E_t \rangle_{res}$ may be estimated by means of the well-known pendulum approximation [41]. Near the

⁺ Higher resonances appear near all values of J_0 commensurate to 2π . At small $|\epsilon|$ such higher-order resonances affect regions of phase space, that are negligibly small with respect to the main resonance. They are altogether ignored in the present discussion. Also note that structures that are small compared to the “Planck constant” $|\epsilon|$ are irrelevant for the purposes of the ϵ -classical approximation.

ϵ SM resonance, the motion is described (in *continuous* time) by the following pendulum Hamiltonian in the canonical coordinates J', ϑ :

$$H_{res} = \frac{1}{2}(J')^2 + |\epsilon|k \cos(\vartheta) . \quad (33)$$

The resonance width δJ_{res} is estimated by the separation (in action) between the separatrices of the pendulum motion. The period of the small pendulum oscillations is $2\pi t_{res}$ where $t_{res} = (k|\epsilon|)^{-1/2}$, so we use t_{res} as a characteristic time scale for the elliptic motion in the resonant zone. One may altogether remove $|\epsilon|$ from the Hamilton equations, by scaling momentum and time by factors $(k|\epsilon|)^{-1/2} = 4/\delta J_{res}$, $(k|\epsilon|)^{1/2} = 1/t_{res}$ respectively. Therefore,

$$\langle (\delta J_t)^2 \rangle = \langle (J'_t - J'_0)^2 \rangle \sim k|\epsilon|G(t\sqrt{k|\epsilon|}) , \quad (34)$$

for an ensemble of orbits started inside the resonant zone, where $G(\cdot)$ is a parameter-free function, whose explicit expression involves elliptic integrals. This function results of averaging over nonlinear pendulum motions with a continuum of different periods, so it saturates to a constant value when the argument is larger than ~ 1 . At small values ($\ll 1$) of the argument it behaves quadratically. The contribution to the total energy is then obtained on multiplying (34) by $|\epsilon|^{-2}\delta J_{res}/(4\pi)$, because only a fraction $\sim \delta J_{res}/(2\pi)$ of the initial ensemble is trapped in the resonant zone. As a result

$$\langle E_t \rangle_{res} \sim \pi^{-1}|\epsilon|^{-1/2}k^{3/2}G(t\sqrt{k|\epsilon|}) . \quad (35)$$

When δJ_{res} is small, $\sin^2(J'/2)$ may be replaced by $J'^2/4$ in the integrand in (32), leading to

$$\Phi(t) \sim \frac{k^2}{4}t \Phi_0(t\sqrt{k|\epsilon|})$$

with

$$\Phi_0(x) \equiv \frac{2}{\pi} \int_0^x ds \frac{\sin^2(s)}{s^2} .$$

Replacing in (31), we obtain:

$$\begin{aligned} R(t, k, \epsilon) &\equiv \frac{\langle E_{t,\epsilon} \rangle}{\langle E_{t,0} \rangle} \sim H(x) \equiv 1 - \Phi_0(x) + \frac{4}{\pi x}G(x) , \\ x &= t\sqrt{k|\epsilon|} = t/t_{res} . \end{aligned} \quad (36)$$

Hence $R(t, k, \epsilon)$ depends on t, k, ϵ only through the scaling variable $x = t/t_{res}$. The width in ϵ of the resonant peak therefore scales like $(kt^2)^{-1}$. The scaling law (36) is demonstrated by numerical data shown in Fig. 5. The function $H(x)$ was numerically computed: in particular, $G(x)$ was computed by a standard Runge-Kutta integration of the pendulum dynamics (33). The scaling function $H(x)$ decays proportional to x^{-1} at large x , because so do $1 - \Phi_0$ and $4G(x)/(\pi x)$; the latter, due to the saturation of G . From Fig. 5 it is seen that Φ_0 is quite slowly varying at $x > 4$. The structures observed in that region are then due to $G(x)$, which describes the resonant island. Numerical computation shows that $G(x)$ saturates via a chain of oscillations of decreasing amplitude around the asymptotic value. These give rise to three local

maxima in the graph of $x^{-1}G(x)$, followed by a chain of gentle oscillations in the tail. The first and most pronounced maximum lies in the small- x region, and is not resolved by the scaling function $H(x)$, apparently because it is effaced by the rapid decay of $1 - \Phi_0(x)$. The subsequent maximum and its symmetric partner at $\epsilon < 0$ are instead resolved and precisely correspond to the “horns” the right-hand one of which is marked by the arrow in Fig. 4. The oscillations in the tail of $x^{-1}G(x)$ are also well reproduced in the tail of $H(x)$.

The scaling law shows that at given k, t the energy curve $\langle E_{t,\epsilon} \rangle$ vs. ϵ decays proportional to $|\epsilon|^{-1/2}$ past the “horns”. As t increases the horns rise higher while moving closer and closer to $\tau = 2\pi$, because they are located at a constant value of $x = t\sqrt{k|\epsilon|}$. Thus an overall $|\epsilon|^{-1/2}$ dependence eventually develops (cf., Figs. 4, 5). In the case when the smooth initial momentum distribution includes values $n_0 \neq 0$ and/or is appreciably non-uniform in quasi-momentum, the statistical weights of the various phase-space regions are different. Scaling in the single variable t/t_{res} still holds, but the scaling functions Φ_0 and G may be different.

This analysis shows that the structure of the resonant peak is essentially determined by the main resonant island of the ϵ SM. It neglects higher-harmonics resonances of the ϵ SM, higher order islands, and especially the growth of the stochastic layer surrounding the main resonance. Such structures grow with $|\epsilon|$ and are expected to introduce deviations from the scaling law (36). Hence this analysis is valid only if $|\epsilon|$ is not too close to the threshold for global chaos $|\epsilon|_{cr} \approx 1/k$. On trespassing this threshold, the *critical regime* of the ϵ SM is entered. No isolating KAM curve survives, so the energy curve rises in time for $|\epsilon| > |\epsilon|_{cr}$. Estimating the mean energy at relatively short times and for $|\epsilon|k < 4.5$ is difficult, because of the coexistence of unbounded, non-homogeneous diffusion and of elliptic motion inside residual stable islands. The increase of the curve with $|\epsilon|$ at constant t is due to the decreasing size of the latter islands, and to the rapid increase of the diffusion coefficient (proportional to $(|\epsilon| - |\epsilon|_{cr})^\gamma$, $\gamma \simeq 3$ at large enough t [42, 43]).

4.1.2. Validity of the ϵ -classical approximation near resonance. The ϵ -quasi-classical approximation is trivially exact at all times for $\epsilon = 0$, as shown above. At nonzero ϵ , it is valid for not too large times t , and it is in the long run spoiled by quantum, non- ϵ -classical effects. At $|\epsilon| < |\epsilon|_{cr}$ the ϵ -classical motion is bounded by KAM curves, so the main quantum mechanism leading to non- ϵ -classical behaviour is tunnelling. Estimating the related time scales is a non-trivial problem, because the 2π -periodicity in action of the ϵ -classical phase space may enhance tunnelling, and even result in delocalization, depending on the degree of commensuration between 2π and the “Planck constant” $|\epsilon|$. For instance, if $|\epsilon|/2\pi$ is rational, then the quantum motion will be ballistic asymptotically in time. This is just the ordinary quantum resonance of the quantum kicked rotor (section 3). In order that one such resonance with $|\epsilon| = 4\pi p/q$ exists at $|\epsilon|$ less than some $|\epsilon|_0$, it is necessary that $q > 4\pi/|\epsilon|_0$. It will show up after a time roughly estimated by $|\epsilon|$ times the inverse bandwidth. The bandwidth is estimated to decrease

faster than exponentially at large q [9, 10], so one may infer that the time of validity of the ϵ -quasi-classical approximation is at least exponentially increasing with $1/|\epsilon|$ as the exact resonance at $\epsilon = 0$ is approached.

At $|\epsilon| > |\epsilon|_{cr}$ the ϵ -classical motion is unbounded, and the difference between ϵ -classical and quantal energy curves vs. τ is basically set by various quantum localization effects, including localization by Cantori close to the $|\epsilon|_{cr}$ [44, 45]. As a consequence, if t is large enough, then the ϵ -classical curve lies much higher than the quantum one. Nevertheless the latter still rises with $|\epsilon|$ at constant t , because of the growth of the localization length (that goes along with the growth of the ϵ -classical diffusion [3]).

5. Decoherence induced by spontaneous emission.

Loosely speaking, decoherence induced by external noise is expected to drive a quantum system towards classical behaviour. One in particular expects the quantum resonances for δ -kicked particles to be strongly impaired, whenever the noise spoils the conservation of quasi-momentum, because that purely quantal conservation law plays a key role in quantum resonances. This is exactly the case when decoherence is induced by Spontaneous Emission (SE) [21, 32, 33, 20, 40, 46]. A beam of nearly resonant light of wave vector \vec{k}_T may induce an internal transition in the atom. The absorbed photon is thereafter spontaneously re-emitted in a random direction, and the whole process results in a random change of the momentum of the centre-of-mass atomic motion. The statistical average of this change equals $\hbar\vec{k}_T$. Although SEs are already produced at a quite small rate by the standing wave which produces the kicks, they have also been experimentally introduced in a controlled way [32, 33] by switching on near-resonant, low-intensity laser beams immediately after each kick. The additional laser beams induced an intensity-dependent mean number n_{SE} of SE events per atom and per kicking period between 0 and 0.2. During each kicking period τ , the SE-inducing laser was active over a (physical) time $\tau_{SE} \approx 0.067\tau$. In our analysis we neglect the delay between absorptions and subsequent SEs. We hence assume that the atom undergoes random momentum changes due to SE at a discrete sequence of random times. Here we are only interested in the projection of such momentum changes onto the kicking direction*. Both the SE times and the corresponding momentum changes are modelled by *classical* random variables, independent of the centre-of-mass motion of the atom. This assumption is reasonable as long as n_{SE} is relatively small; otherwise, the atoms may, in the average, be slowed down or cooled - a velocity-dependent effect, which cannot be accounted for under this assumption. On the other hand, at the high field intensity of a quasi-resonant laser beam which is required for large n_{SE} stimulated emission would prevail. The statistical atom dynamics may be studied by investigating the stochastic Hilbert-space evolution of the atomic state vector [47, 20]‡.

* The effect of randomly induced deviations from the straight line is, however, an interesting question that should be studied separately.

‡ This approach was first implemented for the study of randomized δ -kicked rotor dynamics in ref. [48].

initial incoherent mixture of plane waves with a distribution $f(p_0)$. We further assume that all the variables describing SE events are given and fixed. Their specification defines a *realization* of the random SE events. Then we compute the deterministic evolution of the atomic state vectors up to time t . The quantum probability distribution of an observable in the final state depends on the chosen realization and on the initial state as well; averaging over both yields the final statistical distribution for that observable. The time evolution of distributions and related averages is the object of the following analysis.

5.1. Kicked dynamics in the presence of SE.

Let $|\psi(t)\rangle$ be the state vector of the atom immediately after the t -th kick. Let the integer ν_t denote the number of SEs during the subsequent SE-inducing window. Such events are assumed instantaneous. Denote s_{j-1} the delay (in physical time) of the j -th event with respect to the $(j-1)$ -th one, and d_j the momentum change of the atom induced by the j -th SE. For notational convenience a 0-th fictitious SE is assumed to occur immediately after the t -th kick, and a $(\nu_t + 1)$ -th one immediately before the $(t+1)$ -th kick, with $d_0 = d_{\nu_t+1} = 0$.

The state vector immediately after the $(t+1)$ -th kick is, apart from an inessential phase factor,

$$|\psi(t+1)\rangle = \hat{S}(\delta_t) e^{-ik \cos(\hat{X})} e^{-i\tau(\hat{P} + \chi_t)^2/2} |\psi(t)\rangle, \quad (37)$$

where:

$$\chi_t = \sum_{j=1}^{\nu_t} \frac{s_j}{\tau} \sum_{k=0}^j d_k, \quad \delta_t = \sum_{j=0}^{\nu_t} d_j, \quad \hat{S}(\cdot) = e^{i(\cdot)\hat{X}}. \quad (38)$$

Note that the 1st and the 2nd operator on the rhs of (37) commute. The conservation of quasi-momentum is broken by the operator $\hat{S}(\delta_t)$; however, it may be restored by means of the substitution:

$$|\psi(t)\rangle = \hat{S}(\delta_0 + \delta_1 + \dots + \delta_{t-1}) |\tilde{\psi}(t)\rangle \quad (39)$$

which is a time-dependent, momentum shifting gauge transform; the resulting gauge will be termed the *stochastic gauge* in the following. Replacing (39) in (37), and using

$$e^{-i\tau(\hat{P} + \alpha)^2/2} \hat{S}(\gamma) = \hat{S}(\gamma) e^{-i\tau(\hat{P} + \alpha + \gamma)^2/2},$$

one easily finds:

$$|\tilde{\psi}(t+1)\rangle = e^{-ik \cos(\hat{X})} e^{-i\tau(\hat{P} + \chi_t + \sum_{s=0}^{t-1} \delta_s)^2/2} |\tilde{\psi}(t)\rangle. \quad (40)$$

This evolution does preserve quasi-momentum, so reduction to β -rotor dynamics may be performed as described in section 2, leading to

$$|\tilde{\psi}_\beta(t+1)\rangle = \hat{U}_\beta(t) |\tilde{\psi}_\beta(t)\rangle; \quad \hat{U}_\beta(t) = e^{-ik \cos(\hat{\theta})} e^{-i\tau(\hat{N} + \eta_t)^2/2}, \quad (41)$$

where

$$\eta_t = \beta + \chi_t + \sum_{s=0}^{t-1} \delta_s . \quad (42)$$

In this way the stochastic evolution (38) has been separated in two parts. One of these is described in (39) by the operator \hat{S} ; the other is the evolution (41) in the stochastic gauge. The former is just a translation (in momentum) by the total momentum imparted by SE during the considered time; this part is *totally classical*, so it is the latter part that encodes the coherent stochastic evolution.

5.2. A theoretical model for randomized kicked rotor dynamics.

In experiments, SE occurs at random times within SE-inducing time windows, and there is one such window immediately after each kick. We shall say that a “*SE event*” occurs at the integer time t , whenever *at least one* SE occurs in the window following the t -th kick. In this way, the number of SEs may be larger than the number of SE events. The probability of a SE event is denoted p_{SE} . We then assume:

(S1) SE events occurring at different times are statistically independent. Hence, the random variables δ_t ($t = 0, 1, 2, \dots$) specifying the total (projected) momentum change produced by SE in the t -th kicking period (eq. (38)) are independent, identically distributed random variables.

The following two assumptions are at once the simplest and the strongest possible ones. They were chosen because they greatly simplify the otherwise still possible, yet cumbersome exact solution. Their validity will be discussed in section 5.2.5, where it will be demonstrated that the main results derived below remain unchanged under less stringent and more realistic assumptions.

(S2) The finite duration of the SE-operating windows is negligibly small compared to the kicking period. Hence, $s_{\nu_t} \approx \tau$ while $s_j \approx 0$ for $j < \nu_t$, so that $\chi_t \approx \delta_t$ in (38), and $\eta_t \approx \beta_0 + \sum_0^t \delta_t$ in (42). Different SEs may occur in the same kicking period, each separately contributing to the total momentum change δ_t recorded in that period; nevertheless, their separation in time is neglected.

(S3) The occurrence of a SE event results in total randomization of the quasi-momentum. Given assumption S2, this is equivalent to assuming that the conditional distribution of the variable $\delta_t \bmod(1)$, given that a SE event occurs at time t , is uniform in $[0, 1]$ (in our units). We further assume a zero mean for the distribution of δ_t . While no further specification is needed for the formal elaborations below, in numerical simulations we shall in fact use a uniform conditional distribution in $[-1/2, 1/2]$ (in our units).

(S4) As in the SE-free case, we assume the initial statistical ensemble to be an incoherent mixture of plane waves.

5.2.1. *Random Walk in Hilbert space, at exact resonance.* Assumption (S4) will not be used in this subsection. The results of this subsection may therefore be used under different choices of the initial ensemble. Let SE events occur after $t_0 \equiv 0$ at integer times $t_1 = \Delta_0, t_2 = \Delta_0 + \Delta_1, \dots, t_j = t_{j-1} + \Delta_{j-1}, \dots$. The variables Δ_j , ($j \geq 0$) are integer, independent random variables. Under assumption (S1) they are distributed on the positive integers n with probabilities:

$$\rho(n) = p_{\text{SE}}(1 - p_{\text{SE}})^{n-1} \text{ for } n > 0 \text{ , } \rho(0) = 0 \text{ ,} \quad (43)$$

where p_{SE} is the probability that at least one SE takes place in one kicking period. For all integers $t > 0$ we define $N_t = \max\{j : t_j \leq t\}$, the number of SE events occurring not later than time t , and $N_0 = 0$. The integer random variables N_t , $t \geq 0$ define a Bernoulli process^{††}.

After such preliminaries, we set out to study the evolution in the stochastic gauge, as defined by eqs. (41). The quasi-momentum β of a β -rotor is constant in time, and for each rotor $\eta_0 = \beta$ (SE events are allowed immediately after kicks, and no kick occurs at $t = 0$). In the stochastic gauge, the random propagator from time 0 to time t for the β -rotor is given by the ordered product

$$\hat{U}_{S,\beta}(t) = \prod_{s=0}^{t-1} \hat{U}_{\beta}(s) . \quad (44)$$

The subscript S on the lhs refers to the stochastic gauge. The one-step propagators $\hat{U}_{\beta}(t)$ are defined in eq. (41). Similar to what was done in section 3.1 at *exact resonance* $\tau = 2\pi\ell$ one may write (cf. eq. (7)):

$$\hat{U}_{\beta}(t) = e^{-ik \cos(\hat{\theta})} e^{-i\xi_t \mathcal{N}} \equiv e^{-ik \cos(\hat{\theta})} \hat{\mathcal{R}}(\xi_s) \quad (45)$$

where $\xi_t = \pi\ell(2\eta_t \pm 1)$. Although η_t is not restricted in the interval $[0, 1]$ in eq. (41), the resonance condition allows for ξ_t to be taken in $[-\pi, \pi]$ in (45). Under assumption (S2), ξ_t has a constant value $\tilde{\xi}_j$ in between $t = t_j$ and $t = t_{j+1}$, such that

$$\tilde{\xi}_j \equiv \xi_0 + 2\pi\ell \sum_{m=0}^j \delta_m \text{ mod}(2\pi) \text{ , } -\pi \leq \tilde{\xi}_j < \pi \text{ ,} \quad (46)$$

where δ_m is the total momentum imparted by the m -th SE event. Hence, $\xi_t = \tilde{\xi}_{N_t}$ in between the t -th kick and the $(t + 1)$ -th one. A realization of the SE events is assigned by specifying the values of all the SE random variables just defined, which we collectively denote by the shorthand notations δ for the random momentum shifts and Δ for the random times of SE events. Once the final observation time t and the realization are fixed, for notational convenience we re-define $\Delta_{N_{t-1}} = t - t_{N_{t-1}}$. Replacing (46) in (45), and then in (44), we get

$$\hat{U}_{S,\beta}(t) = \prod_{s=0}^{t-1} e^{-ik \cos(\hat{\theta})} \hat{\mathcal{R}}(\tilde{\xi}_{N_s}) .$$

^{††}This process should not be confused with the continuous Poisson process that may be used for the SEs occurring within *one* and the same kicking period; see subsection 5.2.5.

By repeated use of

$$e^{-ik \cos \hat{\theta}} \hat{\mathcal{R}}(\xi) = \hat{\mathcal{R}}(\xi) e^{-ik \cos(\theta + \xi)} ,$$

eq. (44) may be rewritten in the form:

$$\hat{\mathcal{U}}_{S,\beta}(t) = \hat{\mathcal{R}}(\tilde{\xi}_0 + \tilde{\xi}_{N_1} + \dots + \tilde{\xi}_{N_{t-1}}) e^{-ikF(\hat{\theta}, \delta, \Delta, t)} , \quad (47)$$

where:

$$F(\hat{\theta}, \delta, \Delta, t) = \sum_{s=0}^{t-1} \cos(\hat{\theta} + \sum_{r=0}^s \tilde{\xi}_{N_r}) . \quad (48)$$

We next define $\gamma_j = \sum_{m=0}^{j-1} \Delta_m \tilde{\xi}_m$. Replacing s in (48) by $s = j + l$ with $j = N_s$, and summing over j, l separately,

$$F(\hat{\theta}, \tilde{\xi}, \Delta, t) = \sum_{j=0}^{N_{t-1}} \sum_{l=0}^{\Delta_j - 1} \cos(\hat{\theta} + \gamma_j + l \tilde{\xi}_j) . \quad (49)$$

We further define:

$$z_j = \sum_{r=0}^{\Delta_j - 1} \exp(i\gamma_j + ir \tilde{\xi}_j) ; \quad Z_m = \sum_{j=0}^m z_j ; \quad W_t = Z_{N_{t-1}} , \quad (50)$$

so finally

$$F(\hat{\theta}, \delta, \Delta, t) = |W_t| \cos(\hat{\theta} + \arg(W_t)) .$$

Note that W_t here differs from W_t in eq. (10). Let the initial state of the atom be a plane wave of momentum $p_0 = n_0 + \beta_0$. Given a realization (δ, Δ) , we operate on the corresponding rotor state (5) with the propagator (47). The (random) state of the rotor at time t is given, in the momentum representation, by:

$$\begin{aligned} \langle n | \hat{\mathcal{U}}_{S,\beta_0}(t) \psi_{\beta_0} \rangle &= e^{i\varphi_t} \int_0^{2\pi} \frac{d\theta}{2\pi} e^{-i(n-n_0)\theta - ik|W_t| \cos(\theta)} , \\ \varphi_t &= (n - n_0) \arg(W_t) - n \gamma_{N(t-1)} . \end{aligned} \quad (51)$$

The distribution of momenta n at time t is

$$P(n, t | n_0, \beta_0, \delta, \Delta, N) = J_{n-n_0}^2(k|W_t|) . \quad (52)$$

This is formally identical to (12), but now W_t depends on the initial quasi-momentum β_0 and on the realization of the SE events as well. It is a stochastic process and the random state (51) performs a random walk in the rotor's Hilbert space.

5.2.2. Statistical Averages. Computation of statistical averages requires averaging over the SE random variables (δ, Δ) and over the initial momentum $p_0 = n_0 + \beta_0$. Under our assumptions all such variables are classical random variables. Expectations (resp., conditional expectations) obtained by averaging over such classical variables will be denoted $\mathcal{E}\{.\}$ (resp., $\mathcal{E}\{.\}.$). For instance, $\mathcal{E}\{.|p_0\}$ stands for the average over the SE variables alone, given the value of p_0 (or equivalently of n_0, β_0, ξ_0).

The large- t behaviour of the stochastic process W_t that drives the stochastic rotor evolution is ruled by the large m behaviour of the process Z_m . The properties of the

latter process are completely determined by the assumptions (S2),(S3). Together with eq. (46) assumption (S3) entails that the $\tilde{\xi}_j$ are mutually independent random variables, uniformly distributed in $(-\pi, \pi)$ (with the possible exception of ξ_0 , whose distribution is defined by the initial ensemble). This fact has the following consequences, that are derived in Appendix B: the complex variables z_j are pairwise uncorrelated whenever $j+k > 1$; moreover z_j, z_k are independent whenever $|j-k| \geq 2$. Thus the process Z_m is a random walk in the complex plane, and the distribution of Z_m approaches an isotropic Gaussian distribution in the complex plane as $m \rightarrow \infty$. On account of the properties of the Bernoulli process, the process W_t at large t has quite similar features.

Moments of W_t may be explicitly computed at all t . For instance

$$\begin{aligned} \mathcal{E}\{|W_t|^2 \mid \Delta\} &= \sum_{j,k=0}^{N_{t-1}} \mathcal{E}\{z_j z_k^* \mid \Delta\} \\ &= \sum_{j=0}^{N_{t-1}} \mathcal{E}\{|z_j|^2 \mid \Delta\} + 2\chi(N_{t-1}) \operatorname{Re}(\mathcal{E}\{z_1 z_0^* \mid \Delta\}), \end{aligned} \quad (53)$$

where (B.3) was used, and $\chi(\cdot)$ is the characteristic function of the strictly positive integers. The variables Δ_j were defined such that $\sum_{j=0}^{N_{t-1}} \Delta_j = t$; hence, with the help of (B.3) and (B.4) we find:

$$\mathcal{E}\{|W_t|^2 \mid \Delta\} = \mathcal{M}(\Delta_0) - \Delta_0 + t + 2\chi(N_{t-1}) \operatorname{Re}\mathcal{N}(\Delta_0). \quad (54)$$

Now $\Delta_0 = t_1$ if $t_1 \leq t$ and $\Delta_0 = t$ if $t_1 > t$, with t_1 the time of the 1st SE event. Furthermore, $N_{t-1} = 0$ is equivalent to $t_1 \geq t$, and t_1 is distributed according to (43). Therefore averaging over the random SE times Δ yields:

$$\begin{aligned} \mathcal{E}\{|W_t|^2\} &= t \operatorname{Prob}\{t_1 \leq t\} + \mathcal{M}(t) \operatorname{Prob}\{t_1 > t\} + C(t, p_{\text{SE}}) \\ &= t(1 - q_{\text{SE}}^t) + q_{\text{SE}}^t \mathcal{M}(t) + C(t, p_{\text{SE}}) \end{aligned} \quad (55)$$

where $q_{\text{SE}} = 1 - p_{\text{SE}}$, and

$$C(t, p_{\text{SE}}) = \sum_{n=1}^t \rho(n) [\mathcal{M}(n) - n + 2\operatorname{Re}\mathcal{N}(n)]. \quad (56)$$

With a smooth initial QM distribution (15) it is easily seen from the definitions (B.3) and (B.4) of \mathcal{M} and \mathcal{N} that

$$|C(t, p_{\text{SE}})| \leq 3(\delta f_0) \sum_{n=1}^t n \rho(n), \quad (57)$$

where (δf_0) is the maximum of $|f_0(\beta) - 1|$ in $[0, 1)$. In the case of a uniform initial QM distribution, $\mathcal{M}(t) = t$ and $C(t, p_{\text{SE}}) = 0$, so

$$\mathcal{E}\{|W_t|^2\} = t, \quad (58)$$

like in the case without SE. With a non-uniform initial QM distribution, letting $p_{\text{SE}} \rightarrow 0$ at fixed t causes the 1st and the 3d term on the rhs of (55) to vanish. If instead $t \rightarrow \infty$ at fixed $p_{\text{SE}} > 0$, then the 1st and the 2nd term on the rhs approach t and zero respectively, exponentially fast; the 3d term remains bounded according to (57). So the result which is obtained with a uniform QM distribution is asymptotically approached.

5.2.3. *Growth of energy.* Assuming that the initial state and the SE realization are given, and denoting $\tilde{\delta}_t = \sum_0^{t-1} \delta_s$, the quantum expectation of the energy of the atom at time t may be written as:

$$\begin{aligned} \overline{E}(t) &= \frac{1}{2} \int dp p^2 |\langle p | \psi(t) \rangle|^2 = \frac{1}{2} \int dp (p + \tilde{\delta}_t)^2 |\langle p | \tilde{\psi}(t) \rangle|^2 \\ &= \frac{1}{2} \int dp p^2 |\langle p | \tilde{\psi}(t) \rangle|^2 + \frac{1}{2} \tilde{\delta}_t^2 + \tilde{\delta}_t \int dp p |\langle p | \tilde{\psi}(t) \rangle|^2, \end{aligned} \quad (59)$$

where (39) was used. This expression has to be averaged over the initial statistical ensemble and over all SE realizations. Then

$$\mathcal{E}\{\tilde{\delta}_t^2\} = D(t-1) \quad , \quad \mathcal{E}\{\tilde{\delta}_t\} = 0 \quad , \quad (60)$$

where $D = \mathcal{E}\{\delta_t^2\}$ is the mean square momentum change per period due to Spontaneous Emission. For an initial plane wave (5) of momentum $p_0 = n_0 + \beta_0$, with the help of (52) one finds

$$\begin{aligned} \int dp p |\langle p | \tilde{\psi}(t) \rangle|^2 &= \sum_n \int_0^1 d\beta (n + \beta) |\langle n | \tilde{\psi}_\beta(t) \rangle|^2 \\ &= \sum_n (n + \beta_0) J_{n-n_0}^2(k|W_t|) = n_0 + \beta_0. \end{aligned} \quad (61)$$

where $J_n(\cdot) = (-)^n J_{-n}(\cdot)$ and $\sum_n J_n^2(\cdot) = 1$ were used. Similarly,

$$\int dp p^2 |\langle p | \tilde{\psi}(t) \rangle|^2 = \sum_n (n + \beta_0)^2 J_{n-n_0}^2(k|W_t|) \quad , \quad (62)$$

whence, using (E.2),

$$\int dp p^2 |\langle p | \tilde{\psi}(t) \rangle|^2 = \frac{1}{2} k^2 |W_t|^2 + (n_0 + \beta_0)^2. \quad (63)$$

Replacing (61) in (59), the expectation of the last term in (59) vanishes due to (60). The expectation of (63) is found with the help of (55). Thus finally:

$$\mathcal{E}\{\overline{E}(t) - \overline{E}(0)\} = \frac{1}{4} k^2 [t(1 - q_{\text{SE}}^t) + \mathcal{M}(t)q_{\text{SE}}^t + C(t, p_{\text{SE}})] + \frac{1}{2} D(t-1). \quad (64)$$

This result reduces to the SE-free one eq. (23) for $q_{\text{SE}} = 1$. The term on the rhs which includes k^2 as a factor is the mean energy in the stochastic gauge. With a uniform QM distribution, it reduces to $k^2 t/4$ (cf. (58)). so it does not contain any SE-related parameters, and is in fact identical to the result obtained in the SE-free case (for an initially uniform QM distribution). In experiments, D is typically small (see section 5.2.5), and the QM distribution is practically uniform; so the growth of the mean energy is but weakly affected by SE. However, a similar, albeit cumbersome computation of higher-order moments would reveal sharp differences, which reflect totally different ways of spreading of the momentum distribution in the two cases. At large time, this can be analyzed in detail, as shown in the next section.

Under assumption (S3), the QM distribution of an atom is immediately turned uniform by the first SE event. The time scale for uniformization of the QM distribution is then $t_c = -1/\log(q_{\text{SE}})$. Eq. (64) shows that for $t \gg t_c$ the growth of energy is linear

with the coefficient $k^2/4 + D/2$, like in the case of a uniform QM distribution. On the other hand, since $C(t, p_{\text{SE}})$ is bounded in time, for $(\delta f_0)t_c \ll t \ll t_c$ the growth of energy is dominated by the term $\mathcal{M}(t)$, which is the same as in the SE-free, non-uniform case.

5.2.4. Asymptotic momentum distribution. In this section we assume $n_0 = 0$; averages over initial distributions allowing for $n_0 \neq 0$ may be easily implemented on the final results. We denote $P(p, t)$ the momentum distribution at time t . We show that, as $t \rightarrow \infty$, $P(p, t)$ approaches a Gaussian distribution with mean value 0, in the sense that, for an arbitrary smooth function $\phi(p)$,

$$\lim_{t \rightarrow \infty} \langle \phi \rangle_t \equiv \lim_{t \rightarrow \infty} \int dp P(p\sqrt{t}, t) \phi(p) = \int dp \phi(p) \mathcal{G}_{D+k^2/2}(p) \quad (65)$$

where $\mathcal{G}_{\sigma^2}(p)$ denotes the normal distribution with zero mean and variance σ^2 . To this end we compute:

$$\begin{aligned} \langle \phi \rangle_t &= \mathcal{E} \left\{ \int dp |\langle p | \psi(t) \rangle|^2 \phi(p/\sqrt{t}) \right\} \\ &= \mathcal{E} \left\{ \int dp |\langle p | \tilde{\psi}(t) \rangle|^2 \phi((p + \tilde{\delta}_t)/\sqrt{t}) \right\} \\ &= \mathcal{E} \left\{ \sum_n J_n^2(k|W_t|) \phi((n + \beta_0 + \tilde{\delta}_t)/\sqrt{t}) \right\}. \end{aligned} \quad (66)$$

For $t \gg 1$ one may neglect corrections of order $1/\sqrt{t}$ in the argument of the smooth function ϕ , so

$$\langle \phi \rangle_t \approx \mathcal{E} \left\{ \sum_n J_n^2(k|W_t|) \phi((n + [\tilde{\delta}_t])/ \sqrt{t}) \right\},$$

where $[\cdot]$ denotes the integer part. Asymptotically as $t \rightarrow \infty$, the statistics of W_t are determined by the *fractional* parts of sums of many δ_s (cf. eqs. (46),(50)). Such sums of a large number of independent terms have a broad distribution, so their integer and fractional parts tend to be independent of each other as the number of terms in the sums diverges. The squared Bessel functions and the function ϕ in the last equation may then be separately averaged. Denoting

$$\phi_t(p) \equiv \mathcal{E} \{ \phi(p + [\tilde{\delta}_t]/\sqrt{t}) \} \quad (67)$$

we may write

$$\langle \phi \rangle_t \approx \sum_n \mathcal{E} \{ J_n^2(k|W_t|) \} \phi_t(n/\sqrt{t}). \quad (68)$$

As $t \rightarrow \infty$, the distribution of W_t approaches an isotropic Gaussian distribution in the complex plane centred at 0. The variance is found from (55) to be $\sim t$ at large t . Hence the distribution of $\rho = |W_t|$ is asymptotically at large t given by $dF_t(\rho) = 2t^{-1} \rho d\rho \exp(-\rho^2/t)$. Consequently,

$$\langle \phi \rangle_t \approx \int_0^\infty dF_t(\rho) \sum_n J_n^2(k\rho) \phi_t(n/\sqrt{t})$$

$$= 2 \int_0^\infty dx x e^{-x^2} \sum_n J_n^2(kx\sqrt{t}) \phi_t(n/\sqrt{t}). \quad (69)$$

The integral over ρ is a classical expectation, but the sum over n is a quantum expectation instead. It may be written as:

$$I_t(kx) \equiv \sum_n J_n^2(kx\sqrt{t}) \phi_t(n/\sqrt{t}) = \langle 0 | \hat{\mathcal{K}}^\dagger \phi_t(t^{-1/2} \hat{\mathcal{N}}) \hat{\mathcal{K}} | 0 \rangle, \quad (70)$$

where

$$\hat{\mathcal{K}} = e^{-ikxt^{1/2} \cos(\hat{\theta})}. \quad (71)$$

If we regard $t^{-1/2}$ as the Planck constant, then $t \rightarrow \infty$ is equivalent to a classical limit. In that limit $t^{-1/2} \hat{\mathcal{N}}$ corresponds to (angular) momentum p , and $\hat{\mathcal{K}}$ corresponds to $p \rightarrow p + kx \sin(\theta)$. Therefore, the ‘‘classical’’ limit ($t \rightarrow \infty$) for the momentum distribution in the state $\hat{\mathcal{K}} | 0 \rangle$ is given by the distribution of $kx \sin(\theta)$, with θ uniformly distributed in $[0, 2\pi]$. Replacing the quantum expectation (70) by the average over the related classical distribution yields

$$\lim_{t \rightarrow \infty} I_t(kx) = \int_{-\pi}^{\pi} \frac{d\theta}{2\pi} \phi_\infty(kx \sin \theta) = \int_{-kx}^{kx} \frac{dp}{\pi} \frac{\phi_\infty(p)}{\sqrt{k^2 x^2 - p^2}}. \quad (72)$$

Substituting this in (69), and computing the elementary integral over x gives

$$\lim_{t \rightarrow \infty} \langle \phi \rangle_t = \int_0^\infty dx x e^{-x^2} I_\infty(kx) = \frac{1}{k\sqrt{\pi}} \int dp \phi_\infty(p) e^{-p^2/k^2}. \quad (73)$$

On the other hand, by eq. (67)

$$\phi_\infty(p) = \int dp' \phi(p - p') \mathcal{G}_D(p'),$$

where \mathcal{G}_D is the limit ($t \rightarrow \infty$) normal distribution of $\tilde{\delta}_t/\sqrt{t}$. Recalling (73) and the definition of $\langle \phi \rangle_t$ given in (65) we immediately obtain the result claimed there. Hence, $P(p, t)$ is asymptotically equivalent to a Gaussian with zero mean and variance $k^2 t/2 + Dt$. Being just the leading term in the asymptotic approximation as $t \rightarrow \infty$, this misses those terms in the exact result (64) which are bounded in time. The way (73) was derived from (68) shows that decoherence turns the dynamics classical by causing the effective Planck’s constant to decrease with time. An exact derivation of (73) from (68) is given in Appendix C.

5.2.5. Discussion of the model, and numerical results. We shall now discuss assumptions (S1-3); regarding (S4) see section 3.2.

(S1): The experimental time window for SE: $\tau_{\text{SE}} = 0.067\tau = 0.424$, for $\tau = 2\pi$ (or $4.5\mu\text{sec}$, in the Oxford experiments) is on the one hand very large compared to the time scales given by the Rabi frequency of the used atomic transition and by the inverse SE damping rate [32, 33]. On the other hand, τ_{SE} is very small compared to the kicking period. It is therefore reasonable to neglect memory effects inherent to SE processes [14], so this assumption appears legitimate.

(S2): For the case when SE is induced by the kicking wave itself, this assumption remains valid as long as the δ -kick approximation is valid. For the case of the Oxford experiments it may be to some extent supported by the smallness of $\tau_{\text{SE}}/\tau \simeq 0.067$. It should however be mentioned that the main results of our analysis: (64) and the asymptotically Gaussian distribution still hold in the absence of (S2), though a considerably more involved analysis is required. Rather than delving into such analysis, we support this claim by numerical results to be presented below.

(S3): Complete randomization of quasi-momentum after each SE-inducing cycle occurs when the mean number of SEs per period is large, $n_{\text{SE}} \gg 1$: then effective averaging leads to quasi-independent η_t in (42). If else n_{SE} is small, then complete randomization requires that the conditional distribution of $\delta_t \bmod(1)$ (given that at least one SE occurs in the t -th kicking period) be uniform in $[0, 1]$. On the other hand δ_t is the sum of a random number of momentum changes due to single SEs. If these are assumed independent and identically distributed, then each of them has to be uniformly distributed in some interval of integer width. For a single transition in a 3-dimensional atom, the probability distribution of momentum shifts produced by SEs is not isotropic [49]. This in particular implies that the distribution of single SE, projected momentum shifts δp is *not* uniform. In the case when the SE-inducing beam is orthogonal to the kicking direction, it has the parabolic form:

$$\mathcal{P}_0(\delta p) = \begin{cases} C \left(\frac{9}{8} - \frac{3(\delta p)^2}{2} \right) & , \quad |\delta p| \leq k_T/2k_L \\ 0 & , \quad \text{otherwise,} \end{cases} \quad (74)$$

where C is a normalization constant, and $\vec{k}_T \perp \vec{k}_L$ are the (assumed to be orthogonal) wave vectors of the SE-inducing light and of the kicking light, respectively. This distribution is derived for a situation where SE from a $\Delta m = \pm 1$ atomic transition is induced by circularly polarized light [49]. The allowed change in momentum δp is restricted within the interval $[-k_T/2k_L, k_T/2k_L]$, with $k_T/2k_L \simeq 1/2$ (resulting in $C \simeq 1$) in [32, 33]. With a non-uniform distribution such as (74) some correlation is established between QMs in different kicking periods. The mean momentum change due to absorption followed by SE is $\hbar \vec{k}_T$ for a single SE-inducing beam with wave vector \vec{k}_T . Our assumption of zero mean (along the kicking direction) is justified either when $\vec{k}_T \perp \vec{k}_L$, or when the experimental arrangement uses two or more appropriately directed beams, whereby the atoms may be excited with equal probability. In such cases, the distribution of the projected δp is more complicated (and closer to uniformity) than (74). Since the experiments use a large ensemble of Ce atoms, and SEs involve several hyperfine sublevels [33, 27], the assumption of a nearly uniform distribution of momentum changes seems, however, most appropriate. We shall nonetheless use (74) as a term of comparison in “type (II) simulations” (see below) in order to test the effects of deviations from uniformity. Such numerical data demonstrate that our assumption of a uniform distribution in an exactly integer interval of allowed momentum changes does not affect the results, for experimentally relevant times at least.

For the uniform distribution of δp in the interval $[-1/2, 1/2]$, $\langle \delta p^2 \rangle = 1/12$, so the

coefficient D in (60) is $D = n_{\text{SE}}/12$. With the distribution (74) $\langle \delta p^2 \rangle = 3/40$, and $D = n_{\text{SE}}3/40$. In the theoretical model based on assumption (S2) the distribution of the random times at which single SEs occur within *one* kicking period is totally irrelevant, so p_{SE} and n_{SE} enter as *independent* parameters. They have to be related to each other in order to make contact with experiments. A seemingly natural way assumes a Poisson distribution for the SEs occurring within one operating window, at least for not too large p_{SE} . In that case, $p_{\text{SE}} = 1 - \exp(-n_{\text{SE}})$.

We have performed numerical simulations of two types. Type (I) used all assumptions (S1-4); type (II) had assumptions (S2),(S3) replaced by more realistic ones, allowing e.g. for free evolution in between successive SEs occurring in the same kicking period, and using various distributions of δp , such as (74), as discussed above. Type (I) simulations serve as a demonstration of the theoretical exact results, and much more as a term of comparison with type (II) simulations. The essential agreement between the two types demonstrates that our theoretical conclusions remain valid, under less stringent assumptions. Both types of numerical results were obtained by independently evolving rotors in a given Gaussian ensemble, and by incoherently averaging the final results. Random SE events were simulated as follows. After choosing values for τ_{SE} and $p_{\text{SE}} = 1 - \exp(-n_{\text{SE}})$, random SE times were generated in each kicking period from a Poisson distribution with the characteristic time $\tau_{\text{SE}}/n_{\text{SE}}$ within the time window $(t\tau, t\tau + \tau_{\text{SE}})$. To each random time a random momentum jump was associated, from the chosen distribution (uniform or parabolic). In type (I) simulations, such jumps were added to the quasi-momentum the rotor had at (integer) time t . The integer part of the result determined a corresponding shift in the computational basis of angular momentum eigenstates. The fractional part was used as quasi-momentum for a full one-period free rotor evolution. In type (II), free evolution was allowed in between subsequent SE times. In all cases *the computational basis of momentum eigenstates was chosen as large as possible* in order to model as faithfully as possible the ideal models analyzed in previous sections.

Fig. 6 shows a long-time plot for different rates $p_{\text{SE}} = 0.05 \dots 0.2$, and for the two cases: type (I) with SEs happening immediately after the kicks (a), and type (II) with SEs within a finite time window ($\tau_{\text{SE}} = 0.067\tau = 0.424$ [33]) (b). For $p_{\text{SE}} = 0.2$ data is given in Fig. 6 (c) also for the parabolic distribution (74). The energy growth is *in all cases* linear with the predicted slope $D_{\text{dec}} \simeq k^2/4 + D/2$, as discussed above (see eq. (64)). Fig. 7 presents the coarse-grained momentum distributions $P_n(t)$ (see section 3.2.2) defined as the probability that the momentum p of an atom at time t lies in $[n, n + 1)$ (in our units). They are computed for $\tau = 2\pi$ and different SE rates, SE events immediately after the kicks in type (I), within the time window $\tau_{\text{SE}} = 0.424$ with a uniform distribution, or SEs immediately after kicks with distribution (74) in type (II). With added decoherence, the distribution keeps spreading as a whole all the time, looking more and more Gaussian-like while it flattens out. Further remarks are given in section 6. Apart from statistically induced fluctuations in the wings of the distributions no significant difference between the different simulations (Figs. 6-7) is detectable, and

our conclusions from the preceding subsections remain valid in all cases. We conclude that the results obtained in the work are not very sensitive to assumptions (S1-4) that made the analytical treatment possible.

5.3. ϵ -quasi-classical approximation, in the presence of SE.

The ϵ -quasi-classical approximation introduced in section 4 for the study of the coherent nearly resonant quantum motion is easily adapted to the model in the presence of SE, because the effects of SE were modelled by a totally classical noise. In the stochastic gauge, the ϵ -classical approximation may be implemented in the β -rotor propagators (41) much in the same way as in subsection 4.1. The resulting ϵ -classical map corresponding to (27) is:

$$I_{t+1} = I_t + \tilde{k} \sin(\theta_{t+1}) \quad , \quad \theta_{t+1} = \theta_t \pm I_t + \pi\ell + \tau\eta_t \quad . \quad (75)$$

We now exploit assumption (S2) and write $\eta_t = \beta + \tilde{\delta}_t$, where $\tilde{\delta}_t = \sum_{s=1}^t \delta_s$ is the total momentum imparted by SE up to time t . In order to turn off the stochastic gauge, we need to recover the accumulated SE momentum change, hence we change variables to $I_t^* = I_t + |\epsilon|\tilde{\delta}_t$. The momentum of the atom at time t is then $|\epsilon|^{-1}I_t^* + \beta$, where β is the initial quasi-momentum. Denoting $\eta_t^* = \eta_t + \epsilon\beta/(2\pi\ell)$, a straightforward computation yields:

$$\begin{aligned} I_{t+1}^* &= I_t^* + |\epsilon|\delta_{t+1} + \tilde{k} \sin(\theta_{t+1}) \quad , \\ \theta_{t+1} &= \theta_t \pm I_t^* + \pi\ell + 2\pi\ell\eta_t^* \quad , \\ \eta_{t+1}^* &= \eta_t^* + \delta_{t+1} \quad , \\ \eta_0^* &= \tau\beta/(2\pi\ell) \quad . \end{aligned} \quad (76)$$

The δ_t are independent random variables, whose distribution is determined by the statistics of Spontaneous Emission. Numerical simulations of such noisy ϵ -classical maps are shown in Fig. 8, and very well match with the quantum computations at small $|\epsilon|$. The structure of the resonant peak in the presence of SE may be analytically analyzed, using ideas developed in section 4. Under the substitution $J_t = \pm I_t^* + \pi\ell + 2\pi\ell\eta_t^*$ the map (76) reduces to a noisy ϵ SM, which differs from the ϵ SM by a random shift $\tau\delta_t$ of the action J at each step. We assume an initially uniform QM distribution. At any SE time t_j , the distribution of the ensemble in the phase space of the ϵ SM is reshuffled by the random action change. Under the assumption of homogeneous distribution of single SEs in an interval of integer length, the resulting distribution of $J \bmod(2\pi)$ is approximately homogeneous over the unit cell of the ϵ SM. Such randomization may be assumed to wash out correlations between the past and the subsequent random dynamics. Hence the scaling (36) may be used to write the energy at time t as

$$\langle E_{t,\epsilon} \rangle \sim \frac{k^2}{4} \left\langle \sum_{j=0}^{N_t-1} \Delta_j H(\Delta_j/t_{res}) \right\rangle + \frac{1}{2} D' n_{SE} t \quad ,$$

where $\langle \cdot \rangle$ stands for average over all the Bernoulli realizations of the times of SE events, n_{SE} is the average number of Spontaneous Emissions per period, and $D' = n_{SE}^{-1} \langle \delta_t^2 \rangle$ is

the mean square momentum imparted by a single SE. If t_c is sufficiently large compared to 1, one may replace the Bernoulli process by the continuous time Poisson process with the characteristic time $t_c = -1/(\log(1 - p_{\text{SE}})) = 1/n_{\text{SE}}$. This process has the delays Δ distributed with the density $t_c^{-1} \exp(-\Delta/t_c)$. Its statistics reduces to that of the unit Poisson process ($t_c = 1$) by just rescaling all times by the factor $1/t_c$. This entails

$$\left\langle \sum_{j=0}^{N_{t-1}} \Delta_j H(\Delta_j/t_{\text{res}}) \right\rangle \approx 4t_c Q(t/t_c, t_c/t_{\text{res}}), \quad (77)$$

where

$$Q(u, v) \equiv \frac{1}{4} \left\langle \sum_{j=0}^{N_u^1} \Delta_j^1 H(\Delta_j^1 v) \right\rangle. \quad (78)$$

The superscript 1 specifies that the average is now over the realizations of the unit Poisson process: each realization has the continuous time interval $[0, u]$ divided in subintervals Δ_j^1 by a random number N_u^1 of Poisson events. We are hence led to the following scaling law:

$$\langle E_{t,\epsilon} \rangle \sim D' \frac{t}{2t_c} + k^2 t_c Q\left(\frac{t}{t_c}, \frac{t_c}{t_{\text{res}}}\right) \quad (79)$$

or, equivalently,

$$\frac{2\langle E_{t,\epsilon} \rangle - D't/t_c}{2k^2 t_c} \sim Q(u, v), \quad u = t/t_c, \quad v = t_c/t_{\text{res}}. \quad (80)$$

The scaling function $Q(u, v)$ may be explicitly written in terms of the function $H(x)$ by a routinely calculation reported in Appendix D:

$$4Q(u, v) = uH(uv)e^{-u} + \int_0^u dx e^{-x} x H(xv)(2 + u - x). \quad (81)$$

Limiting behaviours of the scaling function $Q(u, v)$ immediately follow from this equation, or from (78) itself. On one hand, for $u = t/t_c \gg 1$ the rhs in (78) is a sum of a large number $\sim t/t_c$ of terms. In that limit, such terms are quite weakly correlated and may be independently averaged, leading to:

$$u \gg 1 : \quad Q(u, v) \sim \frac{1}{4} u \int_0^\infty dx H(vx) x e^{-x}. \quad (82)$$

On the other hand, for $t/t_c \ll 1$, the sum reduces to the single term $j = 0$, with $\Delta_0^1 = t/t_c$; hence

$$u \ll 1 : \quad Q(u, v) \sim \frac{1}{4} u H(uv). \quad (83)$$

In particular, (83) shows that (79) coincides with (36) in the SE-free limit $t_c \rightarrow \infty$. In the opposite limit, (82) shows that if k is fixed then the width in ϵ of the resonant spike does not shrink any more with time when $t \gg t_c$, and its width thereafter scales like $(t_c^2 k)^{-1}$. The spike is therefore erased (that is, it is absorbed in the background) in the strong noise limit $t_c \sim 1$.

If $f_0(\beta_0)$ is smooth but not uniform, the scaling in absence of SE of the form (36) holds

but with a different scaling function H as explained in subsection 4.1.1. Therefore the arguments of the present subsection leading to (79) should hold also in this case.

Numerical simulations in Fig. 9 satisfactorily support this scaling law. Data are obtained in a similar manner as for the case without SE; however, one of the parameters u, v is varied, while keeping fixed either the other parameter or the ratio u/v . The theoretical scaling function $Q(u, v)$ was numerically computed using in (81) the function $H(x)$ computed as described in section 4.1.1.

6. Reconciliation with experimental results.

In the presence of SE induced decoherence, experimentally measured energies at fixed observation time t_{obs} were found to exhibit resonant peaks near the resonant values $\tau = 2\pi\ell$ (integer multiples of the half-Talbot time [32,33,34,35]) that were *higher* than in the SE-free case. Numerical support for this observation was recently given in [50]. Such observations may have been suggestive of an enhancement of quantum resonances due to decoherence: however, such a phenomenon has no match in the theory developed in the previous sections. This paradox will be resolved in this section. It will be shown that certain restrictions, that are unavoidably present in real experiments, depress the ideal resonant behaviour in a way, that is most severe *in the absence of SE*. So the explanation rather lies with the experimentally measured, SE-free peaks being *lower* with respect to the ideal case, than with the SE ones being higher.

The most important experimental features not taken into account in the foregoing theoretical analysis are:

(I) experimental kicks are not δ -like. The ideal model is then only valid as long as the distance travelled by the atoms over the finite duration t_p of the kick is much smaller than the spatial period of the potential ($t_p = 0.5\mu sec$ in [32, 33]). In our units $\tau_p = t_p\hbar(2k_L)^2/M \simeq 0.047$. At large momenta this requirement is violated, and the atomic motion starts averaging over the potential. The small momentum regime is practically not affected by the replacement of the δ -function by a pulse of finite width. A proper theoretical description demands the δ -kicks in the atomic Hamiltonian to be replaced by appropriately shaped pulses [18]. For large momenta the pulses act adiabatically (if they are smooth), leading to trivial classical and quantum localization [18, 17, 40]. The classical phase space is then filled by KAM tori beyond some large momentum value n_{ref} . For smooth pulses, the momentum n_{ref} is inversely proportional to the duration of the pulse τ_p , and the pre-factor of the proportionality depends on the shape of the pulse [18]. The translational invariance in momentum required for quantum resonances is thus destroyed. The atom dynamics mimics the ideal lowest order resonances for a (possibly long) while [18], but not the higher-order ones whose period (in momentum) is not very small compared to n_{ref} . This is an additional reason preventing experimental detection of high-order resonances, no matter how long the observation time. Fig. 10 shows a simulation for an ensemble of rotors, with a rectangular pulse shape of width τ_p . This does not include the smooth switching

on/off of pulses, as described e.g. in [22]; no substantial difference is however expected in the dynamics on relatively small time scales. In each kicking interval the rotors freely evolved over a physical time $\tau - \tau_p$. During the remaining time τ_p they evolved according to the pendulum Hamiltonian $(\hat{\mathcal{N}} + \beta)^2/2 + k \cos(\hat{\theta})$. The latter evolution was computed by a Trotter-Kato discretization of the Floquet operator (equivalent to replacing the pulse by a thick sequence of δ -subkicks).

(II) The experimental signal-to-noise ratio allows only a finite interval of momenta to be observed; in [33] this border was $n_{cut} = 40$ (data with counteracted gravity). Momenta with $n > n_{cut}$ are not included in the experimental data of [33]. Due to this fact, the theoretical momentum distributions have to be appropriately weighed prior to comparison with experimental ones. The crudest way is cutting the theoretical distributions beyond n_{cut} and renormalizing the probability to 1.

The effect of (I) and (II) on the ideal behaviour discussed in the previous section is easily understood in qualitative terms. We start with the SE-free case. The resonant growth of energy is stopped as soon as the ballistic peak in the tail approaches the closest of the two borders that are the effective cut-offs: (I) n_{ref} and (II) n_{cut} . If this happens earlier than the observation time, then the resonant peak is significantly depressed in comparison to the ideal case. We shall presently argue that such depression is mainly due to the cut-off (II) for the experimental cases of [33, 27].

In the case of a rectangular pulse, n_{ref} is not a precisely defined quantity, due to the slow decay of the Fourier harmonics of the pulse. It has to be meant in an effective sense. We hence resort to numerical simulations. In Fig. 10 numerically computed momentum distributions are compared with those obtained in the ideal δ -kicked rotor case; according to such data, the effective n_{ref} should be located in the momentum range 70 – 120.

The second cut-off n_{cut} is simulated by not counting momenta higher than n_{cut} when calculating energies, momentum distributions etc. (the computational basis of momentum eigenstates is however much larger than n_{cut}). Following experimental parameters [33, 27] we choose $n_{cut} = 40$, the distributions are renormalized to unity after disregarding states with momenta larger/smaller than $n = \pm 40$. In Fig. 11 the effect of this cut-off on the growth of the mean energy is shown. In the presence of n_{cut} the deviation from the ideal case appears somewhat earlier, as expected from $n_{cut} < n_{ref}$; moreover, the deviation at $t \gtrsim 20$ is strongly enhanced in the presence of n_{cut} (and in the absence of SE). As shown in Fig. 12 (a), the momentum distributions including both cut-offs (I) and (II) are stable in time, not moving at all in the centre around $n = 0$. The slight enhancement at $|n| \simeq 15 - 40$ as compared to the case without cut-offs (shown in Fig. 10) is only due to n_{ref} which to some extent acts like a reflecting boundary. The ballistic peak, however, which moves in momentum like $n \sim \pi kt/2$ (see discussion after (22)) is lost already after about $t \simeq 40/k \simeq 16$ kicks, cf., Fig. 11. The peak is then beyond the cut-off (II). The estimated loss after about 16 kicks is in correspondence with the saturation of the mean energy vs. time at quantum resonance which has been observed in [32, 27] for $t > 15$ in the experimental results, and in the

theoretical modelling as well (Fig. (4) in [32]).

The dependence of the mean energy on the kicking period τ , which was shown in Fig. 3 for the ideal case of δ -kicks and no cut-offs, is strongly influenced by the cut-offs at exact resonance. This dependence in the absence of SE, with rectangular pulses and cutoff at n_{cut} is shown in Fig. 13(a). By comparing to Fig. 3, we directly see that the only substantial difference is at resonant values $\tau = 2\pi, 4\pi, 6\pi$: cut-offs lead to lower resonant peaks. When the cut-off (II) $n_{cut} = 40$ is applied in the ideal case of δ -kicks, no differences can be detected from the results plotted in Fig. 13(a), again confirming that cut-off (II) is the crucial one. The resonance peaks are smaller, because the resonant growth of energy stops, as soon as the ballistically moving rotors hit the boundary (cf., Fig. 11). Then the mean energy very quickly falls below its ideal value (after about 16 kicks in the plotted case), as can be seen in Fig. 11.

Added SE totally changes this picture. The energy growth is now due to the overall broadening of the distribution, and not just to the ballistic peaks in the tail, as can be seen comparing the various parts of Fig. 7, where kicks are δ -like, and no cutoff is present. The distributions with weak SE are broader in the tails as compared to those with strong SE; the latter are however flatter in the centre, which is why they have roughly the same rms deviation. As already commented, in the SE-free case the quasi-momentum is constant in time, and atoms with quasi-momenta close to $1/2$ travel faster, thus producing the long tails and the ballistic peaks at their edges. In the presence of SE, no atom may persist a long time in the fast-travelling quasi-momentum range, whence it is removed the sooner, the larger p_{SE} . Due to this reason, with SE the cut-offs are “felt” much later by the evolving distribution (Fig. 12, 7). Whereas the cutoff still prevent observation of the fastest atoms, they do not significantly affect the growth of energy until large times. Even then, the momentum distribution normalized within $|n| < n_{cut}$ approaches the flat distribution in $|n| < n_{cut}$ (Fig. 12(b,c,d)), which has a limit value for the second moment significantly higher than the SE-free steady state distribution in the presence of the cutoff.

In contrast to the SE-free case, the dependence of the mean energy on the kicking period τ after 30 kicks is but slightly affected by the cutoffs when SE is present. This is shown in Fig. 13 (b)(c), to be compared to Fig. 3(b). In the experiments (Fig. (2) in [32], Fig. (6) in [33]), the peaks for all cases (a)-(c) are still smaller than in our Fig. 13, which can be explained by the extreme sensitivity of the energy at exact resonance to all sort of perturbations besides those included in our present analysis, and also by difficulties in experimentally tuning to the exactly resonant values of τ . Additional experimental restrictions, e.g., the experienced fluctuations of the potential depth and the resulting averaging over slightly different experimental realizations [33, 27, 46], may lead to a further reduction of the peak, especially in the case without decoherence which is most sensitive to any kind of disturbance.

Acknowledgments

We thank Andreas Buchleitner, Michael d'Arcy, Gil Summy, and Gregor Veble for stimulating comments. S. W. appreciated detailed discussions with Vyacheslav Shatokhin on the atomic decoherence process. The work was supported by the EU program QTRANS RTN1-1999-08400 (S. W.), by the US-Israel Binational Science Foundation (BSF), by the Minerva Center of Nonlinear Physics of Complex Systems, and by the fund for Promotion of Research at the Technion (S. F.).

Appendix A. Analysis of the Steady State Distribution (20).

Appendix A.1. Proof of estimate (21).

From (20) it follows that

$$\sum_{|n| \geq N} M_n^*(t) = \frac{1}{2\pi^2} \int_{-\pi}^{\pi} dx \int_{-\pi/2}^{\pi/2} d\alpha \sum_{|n| \geq N} J_n^2(z) , \quad z := k \sin(x) \csc(\alpha). \quad (\text{A.1})$$

for any positive integer N . In Appendix A.2 we show that:

$$\sum_{|n| \geq N} J_n^2(z) \leq 2 \left(\frac{ez}{2N} \right)^{2N} , \quad (\text{A.2})$$

We choose $0 < \epsilon < \pi$ and we use (A.2) to bound the sum in the inner integral in (A.1) when $|\alpha| > \epsilon/2$; otherwise we use the upper bound 1. Noting that $|z| < \pi k/(2\epsilon)$ whenever $\pi/2 > |\alpha| > \epsilon$,

$$\sum_{|n| \geq N} M_n^*(t) \leq \frac{\epsilon}{\pi} + 2 \left(\frac{k'e}{2N\epsilon} \right)^{2N} . \quad (\text{A.3})$$

where $k' := k\pi/2$. We now minimize the rhs by choosing

$$\epsilon = \frac{ek'}{2N} \left(\frac{8\pi N^2}{ek'} \right)^{\frac{1}{2N+1}} \quad (\text{A.4})$$

(which is indeed not larger than π whenever $N > k \times 1.03\dots$). Replacing (A.4) in (A.3) yields the estimate (21).

Appendix A.2. Proof of ineq. (A.2).

Using the bound (E.6) and the power series expansion of Bessel functions [51],

$$\sum_{n=0}^{\infty} J_n^2(z) e^{nr} \leq \sum_{n=0}^{\infty} \left(\frac{|z|e^{r/2}}{2} \right)^{2n} \frac{1}{(n!)^2} = J_0(i|z|e^{r/2}) \leq e^{|z|e^{r/2}} , \quad (\text{A.5})$$

for any real r . It follows that:

$$\sum_{n=N}^{\infty} J_n^2(z) \leq e^{-Nr} e^{|z|e^{r/2}} ,$$

Ineq. (A.2) follows upon optimizing with respect to r .

Appendix A.3. Proof of the asymptotic formula (22).

For $z \in [-1, 1]$ we define:

$$f(z) := \frac{1}{2\pi} \int_{-\pi/2}^{\pi/2} d\alpha J_0^2(kz \csc(\alpha)) \text{ for } z \neq 0 ; \quad f(0) = \frac{1}{2} . \quad (\text{A.6})$$

The integrand in (A.6) is meant = 0 for $\alpha = 0, z \neq 0$. Using the integral identity (E.3) for Bessel functions, (20) may be rewritten as:

$$M_n^* = \frac{1}{\pi} \int_0^{2\pi} dx \cos(2nx) f(\sin(x)) , \quad (\text{A.7})$$

so, for $|n| > 0$, M_n^* is the $2n$ -th coefficient in the cosine expansion of $f(\sin(x))$. The function $f(z)$ is differentiable in $[-1, 1] \setminus \{0\}$. It will be presently shown that

$$f'(0+) = \lim_{z \rightarrow 0+} f'(z) = -\frac{4k}{\pi^2} \neq 0 .$$

Since $f(z)$ is an even function, it will follow that its first derivative is discontinuous at $z = 0$. We choose $\epsilon > 0$ and write

$$f(z) = f_\epsilon(z) + g_\epsilon(z) , \quad f_\epsilon(z) := \frac{1}{2\pi} \int_{-\epsilon}^{\epsilon} d\alpha J_0^2(kz \csc(\alpha)) . \quad (\text{A.8})$$

Then g_ϵ is differentiable around 0, with $g'_\epsilon(0) = 0$. Hence, $f'(0+) = f'_\epsilon(0+)$. Next we note that if $z > 0$,

$$f'_\epsilon(z) = \pi^{-1} z^{-1} \int_{-\epsilon}^{\epsilon} d\alpha F(kz \csc(\alpha)) ,$$

where $F(x) := xJ_0(x)J'_0(x)$. Noting that

$$|\csc(\alpha) - \alpha^{-1}| < c_1 \alpha$$

for $0 < |\alpha| < \pi/2$ and some numerical constant c_1 , one easily finds

$$\begin{aligned} f'_\epsilon(z) &= \pi^{-1} z^{-1} \int_{-\epsilon}^{\epsilon} d\alpha F(kz \alpha^{-1}) + O(\epsilon) \\ &= -2k\pi^{-1} \int_{kz/\epsilon}^{\infty} du u^{-1} J_0(u) J_1(u) + O(\epsilon) , \end{aligned} \quad (\text{A.9})$$

where $J'_0(z) = -J_1(z)$ was used. Letting $z \rightarrow 0+$ and thereafter $\epsilon \rightarrow 0+$ we obtain:

$$f'(0+) = \lim_{\epsilon \rightarrow 0+} f'_\epsilon(0+) = -2k\pi^{-1} \int_0^{\infty} du u^{-1} J_0(u) J_1(u) = -\frac{4k}{\pi^2} .$$

The integral was computed by using (E.5) and then formula 11.4.36 in [51].

Next we recall from (A.7)

$$f(\sin x) = \frac{1}{2} M_0^* + \sum_{n=1}^{\infty} M_n^* \cos(2nx) .$$

According to the above analysis, the derivative of this function jumps by $-8k/\pi^2$ at $x = j\pi$ (j any integer). Hence the 2nd derivative has the singular part $-8k\pi^{-2} \sum_j \delta(x - j\pi)$, leading to the asymptotic value $-16k\pi^{-3}$ for the coefficients in its cosine expansion. This yields

$$M_n^* \sim \frac{4k}{\pi^3 n^2} \text{ as } n \rightarrow \infty . \quad (\text{A.10})$$

Appendix B. Statistics of the process Z_m .

Appendix B.1. Independence of the variables z_j .

We show that, for any integers n, m , ($m > n$), the variables (z_n, \dots, z_m) are independent of the variables (z_0, \dots, z_k) whenever $k \leq n - 2$. It suffices to show that (z_n, \dots, z_m) are independent of $(\tilde{\xi}_0, \dots, \tilde{\xi}_k, \Delta_0, \dots, \Delta_k)$. To see this, let f be an arbitrary (Borel) function of $m - n + 1$ complex variables, and consider:

$$\mathcal{M}_k \equiv \mathcal{E}\{f(z_n, \dots, z_m) | \tilde{\xi}_0, \dots, \tilde{\xi}_k, \Delta_0, \dots, \Delta_k\}. \quad (\text{B.1})$$

Looking at (50), and recalling that the $\tilde{\xi}_j$ are mutually independent, one notes that (z_n, \dots, z_m) depend on $\tilde{\xi}_j, \Delta_j$ ($0 \leq j \leq k$) through the factor $\exp(i \sum_0^k \tilde{\xi}_j \Delta_j)$, hence only through $\sum_0^k \tilde{\xi}_j \Delta_j \pmod{2\pi}$. Therefore, (B.1) is a function of the variable $\mu_k \equiv \sum_0^k \tilde{\xi}_j \Delta_j \pmod{2\pi}$ alone: $\mathcal{M}_k = \mathcal{M}_k(\mu_k)$. Furthermore, since $k + 1 < n$,

$$\begin{aligned} \mathcal{M}_k(\mu_k) &= \int dP(\tilde{\xi}_{k+1}, \Delta_{k+1}) \mathcal{M}_{k+1}(\mu_{k+1}) \\ &= \int dP(\xi_{k+1}, \Delta_{k+1}) \mathcal{M}_{k+1}(\mu_k + \tilde{\xi}_{k+1} \Delta_{k+1}) \end{aligned} \quad (\text{B.2})$$

because $\tilde{\xi}_{k+1}, \Delta_{k+1}$ are independent of past variables; here $dP(., .)$ is their joint distribution. Now $\tilde{\xi}_{k+1}$ is independent of the integer Δ_{k+1} , and it is uniformly distributed in $(-\pi, \pi)$. Then the integral does not depend on μ_k , so

$$\mathcal{E}\{f(z_n, \dots, z_m) | \tilde{\xi}_0, \dots, \tilde{\xi}_k, \Delta_0, \dots, \Delta_k\} = \mathcal{E}\{f(z_n, \dots, z_m)\},$$

which proves the announced independence property.

Appendix B.2. Correlations of variables z_j .

We prove that, for any $j, k \geq 0$ such that $j + k > 1$

$$\mathcal{E}\{z_j z_k^* | \Delta\} = \delta_{jk} \Delta_j, \quad \mathcal{E}\{z_j z_k | \Delta\} = 0. \quad (\text{B.3})$$

whereas

$$\begin{aligned} \mathcal{E}\{z_1 z_0^* | \Delta\} &= \mathcal{N}(\Delta_0) \equiv \sum_{j=1}^{\Delta_0} \int_{-\pi}^{\pi} dP(\xi_0) e^{ij\xi_0}, \\ \mathcal{E}\{|z_0|^2 | \Delta\} &= \mathcal{M}(\Delta_0) \equiv \int_{-\pi}^{\pi} dP(\xi_0) \frac{\sin^2(\xi_0 \Delta_0 / 2)}{\sin^2(\xi_0 / 2)} \end{aligned} \quad (\text{B.4})$$

where

$$dP(\xi_0) = (2\pi\ell)^{-1} d\xi_0 \sum_{j=0}^{\ell-1} f_0(\beta_j), \quad \beta_j \equiv \frac{\xi_0}{2\pi\ell} + \frac{1}{2} + \frac{j}{\ell} \pmod{1}. \quad (\text{B.5})$$

is the distribution of ξ_0 and f_0 is the probability density of the initial quasi-momentum (15).

In order to show (B.3), we denote:

$$\alpha_j = e^{i\tilde{\xi}_j} \quad , \quad \varphi_j = \sum_{r=0}^{\Delta_j-1} \alpha_j^r$$

so that:

$$z_j z_k^* = \varphi_j \varphi_k^* \prod_{l=0}^{j-1} \alpha_l^{\Delta_l} \prod_{m=0}^{k-1} \alpha_m^{-\Delta_m}. \quad (\text{B.6})$$

Let $j > k$, $j+k > 1$, Then $j > 1$, and the 1st product has the factor $\alpha_{j-1}^{\Delta_{j-1}}$. Hence (B.6) depends on $\tilde{\xi}_{j-1}$ via this factor alone (if $j \neq k+1$) or via this factor multiplied by φ_{j-1}^* (if $j = k+1$), leading to a factor $e^{i\tilde{\xi}_{j-1}(\Delta_{j-1}-l)}$ with $l \leq \Delta_{j-1}-1$. In both cases averaging over $\tilde{\xi}_{j-1}$ yields zero because $\tilde{\xi}_{j-1}$ is uniformly distributed whenever $j > 1$. The case $j < k$ is recovered by complex conjugation. The 2nd equality in (B.3) is straightforward. If $j = k$, then from (50) it follows that

$$\mathcal{E}\{|z_j|^2|\Delta\} = \int_{-\pi}^{\pi} dP(\xi_j) \frac{\sin^2(\xi_j \Delta_j/2)}{\sin^2(\xi_j/2)}. \quad (\text{B.7})$$

where $dP(\xi_j)$ is the distribution of ξ_j . For $j > 0$, $dP(\xi_j) = d\xi_j/(2\pi)$, and the integral is computed according to (E.7). The 1st equation in (B.4) results of a straightforward calculation using the definitions (50) of z_0 and z_1 .

Appendix B.3. Central Limit property.

The properties of the process Z_m allow to conclude that its distribution is asymptotically Gaussian, thanks to known results about the Central Limit Theorem for weakly dependent sequences [52]. Isotropy of the limit Gaussian distribution easily follows from computing $\mathcal{E}\{\text{Re}^2(\sum_j^N e^{-i\theta} z_j)\}$ (the mean square displacement along the direction θ in N steps). Using (B.3), the result is independent of θ .

Appendix C. Gaussian asymptotics for momentum distributions.

Throughout this appendix, the Fourier transform of a function f is denoted by \hat{f} . Notations are otherwise identical to those in section 5.2.4. In particular,

$$\phi_t(n/\sqrt{t}) = \frac{1}{\sqrt{2\pi}} \int du \hat{\phi}_t(u) e^{inu/\sqrt{t}}.$$

Replacing this in (69), and using the Bessel function identity (E.4),

$$\begin{aligned} \langle \phi \rangle_t &= \frac{1}{\sqrt{2\pi}} \int_0^\infty dF_t(\rho) \int du \hat{\phi}_t(u) J_0(2k\rho \sin(u/2\sqrt{t})) \\ &= \frac{2}{\sqrt{2\pi}} \int_0^\infty dx x e^{-x^2} \int du \hat{\phi}_t(u) J_0(2kx\sqrt{t} \sin(u/2\sqrt{t})) \end{aligned} \quad (\text{C.1})$$

which in the limit $t \rightarrow \infty$ yields

$$\langle \phi \rangle_\infty = \frac{2}{\sqrt{2\pi}} \int_0^\infty dx x e^{-x^2} \int du \hat{\phi}_\infty(u) J_0(kxu).$$

Substitution of

$$\hat{\phi}_\infty(u) = \frac{1}{\sqrt{2\pi}} \int dp \phi_\infty(p) e^{-ipu} \quad (\text{C.2})$$

and of (E.5) yields the $t \rightarrow \infty$ limit:

$$\langle \phi \rangle_\infty = 2\pi^{-1} \int_0^\infty dx x e^{-x^2} \int_{-kx}^{kx} dp \frac{\phi_\infty(p)}{\sqrt{k^2 x^2 - p^2}}.$$

Interchanging integrals, we obtain the same result found in the text (equation (73)) by different means.

Appendix D. Derivation of eq. (81).

Let Δ_j^1 , ($j = 0, 1, \dots$) be real nonnegative, independent random variables exponentially distributed with $\mathcal{E}\{\Delta_j^1\} = 1$. For j a nonnegative integer denote $s_j = \sum_{k=0}^j \Delta_k$, and $s_{-1} \equiv 0$. For given $u > 0$ let $N_u^1 \equiv \max\{j : s_j < u\}$. We shall compute the expectation of the random variable

$$f_u \equiv \sum_{j=0}^{N_u^1} f(\Delta_j^1) + f(u - s_{N_u^1}), \quad (\text{D.1})$$

where $f(x)$ is a given nonrandom function; the sum in eq. (78) is of this form, with $f(x) = xH(xv)$. We write $f_u = \sum_{j=0}^\infty f_{u,j}$, where

$$f_{u,j} \equiv \chi(u - s_{j-1})[\chi(u - s_{j-1} - \Delta_j^1)f(\Delta_j^1) + \chi(\Delta_j^1 + s_{j-1} - u)f(u - s_{j-1})], \quad (\text{D.2})$$

and $\chi(\cdot)$ is the unit step function. Then, denoting $G(x) = \int_0^x ds f(s)e^{-s}$,

$$\mathcal{E}\{f_{u,j}|s_{j-1}\} = \chi(r)[G(r) + f(r)e^{-r}] \quad , \quad r = u - s_{j-1}. \quad (\text{D.3})$$

Therefore,

$$\begin{aligned} \mathcal{E}\{f_u\} &= \sum_{j=0}^\infty \mathcal{E}\{\mathcal{E}\{f_{u,j}|s_{j-1}\}\} = G(u) + f(u)e^{-u} + \\ &+ \sum_{j=1}^\infty \int_0^u dP_j(x) [G(u-x) + f(u-x)e^{x-u}], \end{aligned} \quad (\text{D.4})$$

where $dP_j(x) = dx e^{-x} x^{j-1}/(j-1)!$ is the distribution of s_{j-1} for $j > 0$. Summing over j and replacing the definition of $G(x)$ we finally obtain

$$\mathcal{E}\{f_u\} = 2 \int_0^u dx e^{-x} f(x) + f(u)e^{-u} + \int_0^u dx e^{-x} f(x)(u-x). \quad (\text{D.5})$$

Eq. (81) in the text is obtained on substituting $f(x) = xH(xv)$.

Appendix E. Some formulae used in the text.

The following formulas involving Bessel functions were used in the text and previous appendices, these are taken from [51] or derived from formulas there (we give the corresponding numbers in []):

$$\frac{1}{2\pi} \int_{\alpha}^{\alpha+2\pi} d\theta e^{iz \cos \theta} e^{-in\theta} = i^n J_n(z) \quad [9.1.21] \quad (\text{E.1})$$

$$\sum_{n=-\infty}^{\infty} n^2 J_n^2(x) = \frac{1}{2} x^2 \quad [9.1.76] \quad (\text{E.2})$$

$$\int_0^{2\pi} dx J_n^2(b \sin(x)) = \int_0^{2\pi} dx \cos(2nx) J_0^2(b \sin(x)) \quad [11.4.7/8] \quad (\text{E.3})$$

$$\sum_n J_n^2(z) e^{int} = J_0(2z \sin(t/2)) \quad [11.4.8] \quad (\text{E.4})$$

$$J_0(z) = \frac{1}{\pi} \int_{-1}^1 dx \frac{\cos(zx)}{\sqrt{1-x^2}} \quad [9.1.18] \quad (\text{E.5})$$

$$|J_n(z)| \leq \frac{1}{n!} \left| \frac{z}{2} \right|^{|n|} e^{\mathcal{I}m(z)} \quad [9.1.62] . \quad (\text{E.6})$$

The following integral was used in calculating moments of energy:

$$\int_0^{2\pi} dx \frac{\sin^2(tx)}{\sin^2(x)} = 2\pi t . \quad (\text{E.7})$$

References

- [1] Casati G, Chirikov B V, Ford J, and Izrailev F M 1979 in *Stochastic Behavior in Classical and Quantum Hamiltonian Systems* Vol. 93 of *Lecture Notes in Physics* edited by Casati G and Ford J (Springer-Verlag: Berlin) p 334
- [2] Fishman S, Grepel D R, and Prange R E 1982 *Phys. Rev. Lett.* **49** 509
- [3] Chirikov B V and Shepelyansky D L 1986 *Radiofizika* **29** 1041
- [4] Casati G, Guarneri I, and Shepelyansky D L 1988 *IEEE J. Quantum Electron.* **24** 1420
- [5] Galvez E J, Sauer J E, Moorman L, Koch P M, and Richards D 1988 *Phys. Rev. Lett.* **61** 2011
- [6] Bayfield J E, Casati G, Guarneri I, and Sokol D W 1989 *Phys. Rev. Lett.* **63** 364
- [7] Arndt M, Buchleitner A, Mantegna R N, and Walther H 1991 *Phys. Rev. Lett.* **67** 2435
- [8] Fishman S 1993 in *Quantum Chaos*, Vol. Course CXIX of *Proceedings of the International School of Physics "E. Fermi"* edited by Casati G, Guarneri I, and Smilansky U (North Holland: Amsterdam) p 187
- [9] Izrailev F M and Shepelyansky D L 1980 *Theor. Math. Phys.* **43** 353
- [10] Izrailev F M 1990 *Phys. Rep.* **196** 299
- [11] Casati G and Guarneri I 1984 *Commun. Math. Phys.* **95** 121
- [12] Bellissard J and Barelli A, 1992 in *Quantum Chaos – Quantum Measurement* NATO Advanced Research Workshop Copenhagen 1991 edited by Cvitanović P, Persival I, and Wirzba A (Kluwer: Dordrecht) p 105
- [13] Moore F L, Robinson J C, Bharucha C F, Williams P E, and Raizen M G, *Phys. Rev. Lett.* **73** 2974
- [14] Cohen-Tannoudji C, Dupont-Roc J, and Grynberg G 1992 *Atom-Photon Interactions, Basic Processes and Applications* (John Wiley & Sons: New York)

- [15] Graham R, Schlautmann M, and Zoller P 1992 *Phys. Rev. A* **45** R15
- [16] Arndt M, Dahan M B, Guéry-Odelin D, Reynolds M W, and Dalibard J 1997 *Phys. Rev. Lett.* **79** 625
- [17] Klappauf G B, Oskay W H, Steck D A, and Raizen M G 1999 *Physica D* **131** 78
- [18] Blümel R, Fishman S, and Smilansky U 1986 *J. Chem. Phys.* **84** 2604
- [19] Bharucha C F, Robinson J C, Moore F L, Sundaram B, Niu Q, and Raizen MG 1999 *Phys. Rev. E* **60** 3881
- [20] Ammann H, Gray R, Shvarchuck I, and Christensen N 1998 *Phys. Rev. Lett.* **80** 4111
- [21] Klappauf B G, Oskay W H, Steck D A, and Raizen M G 1999 *Phys. Rev. Lett.* **81** 1203
- [22] Steck D A, Milner V, Oskay W H, and Raizen M G 2000 *Phys. Rev. E* **62** 3461
- [23] Milner V, Steck D A, Oskay W H, and Raizen M G 2000 *Phys. Rev. E* **61** 7223
- [24] Godun R M, d'Arcy M B, Oberthaler MK, Summy G S, and Burnett K 2000 *Phys. Rev. E* **62** 013411
- [25] Fishman S, Guarneri I, and Rebuzzini L 2002 *Phys. Rev. Lett.* **89** 084101
- [26] Fishman S, Guarneri I, and Rebuzzini L 2002 *preprint nlin.CD/0205006*
- [27] d'Arcy MB 2002 Ph.D. thesis University of Oxford (Oxford)
- [28] Schlunk S, d'Arcy M B, Gardiner S A, Cassettari D, Godun R M, and Summy G S 2002 *preprint physics/0207075*
- [29] d'Arcy M B, Godun R M, Cassettari D, and Summy GS 2002 *preprint physics/0208104*
- [30] Wimberger S, Guarneri I, and Buchleitner A in preparation
- [31] Oskay W H, Steck D A, Milner V, Klappauf B G, and Raizen M G 2000 *Opt. Commun.* **179** 137
- [32] d'Arcy M B, Godun RM , Oberthaler M K, Cassettari D, and Summy G S, *Phys. Rev. Lett.* **87** 074102
- [33] d'Arcy M B, Godun R M, Oberthaler M K, Summy G S, Burnett K, and Gardiner S A, *Phys. Rev. E* **64** 056233
- [34] Dubetsky B and Berman P R 1997 *Atomic interferometry* Vol. 37 of *Adv. At. Mol. Phys., supplement 3* (Academic Press: Chestnut Hill) p 407
- [35] Goodman J W 1996 *Introduction to Fourier Optics* 2 ed. (McGraw-Hill: New York) p 87
- [36] Blümel R, Buchleitner A, Graham R, Sirko L, Smilansky U, and Walther H 1991 *Phys. Rev. A* **44** 4521
- [37] Hornberger K and Buchleitner A 1998 *Europhys. Lett.* **41** 383
- [38] Buchleitner A, Delande D, and Zakrzewski J 2002 *Phys. Rep.* **368** 409 and references therein
- [39] Izrailev F M 1986 *Phys. Rev. Lett.* **56** 541
- [40] Doherty A C, Vant K, Ball G, Christensen N, and Leonhardt R 2000 *J. Opt. B* **2** 605
- [41] Lichtenberg A J and Lieberman M A 1992 *Regular and Chaotic Dynamics*, Vol. 38 of *Applied Mathematical Sciences* (Springer-Verlag: Berlin)
- [42] MacKay R S, Meiss J D, and Percival I C 1984 *Phys. Rev. Lett.* **52** 697
- [43] Dana I and Fishman S 1985 *Physica D* **17** 63
- [44] Grepel D R, Fishman S, and Prange R E 1984 *Phys. Rev. Lett.* **53** 1212
- [45] Fishman S, Grepel D R, and Prange R E 1987 *Phys. Rev. A* **36** 289
- [46] Williams M E, Sadgrove M P, Daley A J, Gray R N, Tan S M, Parkins AS, Leonhardt R, and Christensen N 2002 *preprint quant-ph/0208090*
- [47] Graham R and Miyazaki S 1996 *Phys. Rev. A* **53** 2683
- [48] Guarneri I 1984 *Lett. Nuovo Cim.* **40** 171
- [49] Mandel L and Wolf E 1997 *Optical Coherence and Quantum Optics*, 1 ed. (CUP: Cambridge)
- [50] Daley A J, Parkins A S, Leonhardt R, and Tan S M 2002 *Phys. Rev. E* **65** 035201(R)
- [51] Abramowitz M and Stegun I A 1972 *Handbook of mathematical functions* (Dover: New York)
- [52] Serfling R J 1968 *Ann. Math. Stat.* **39** 1158

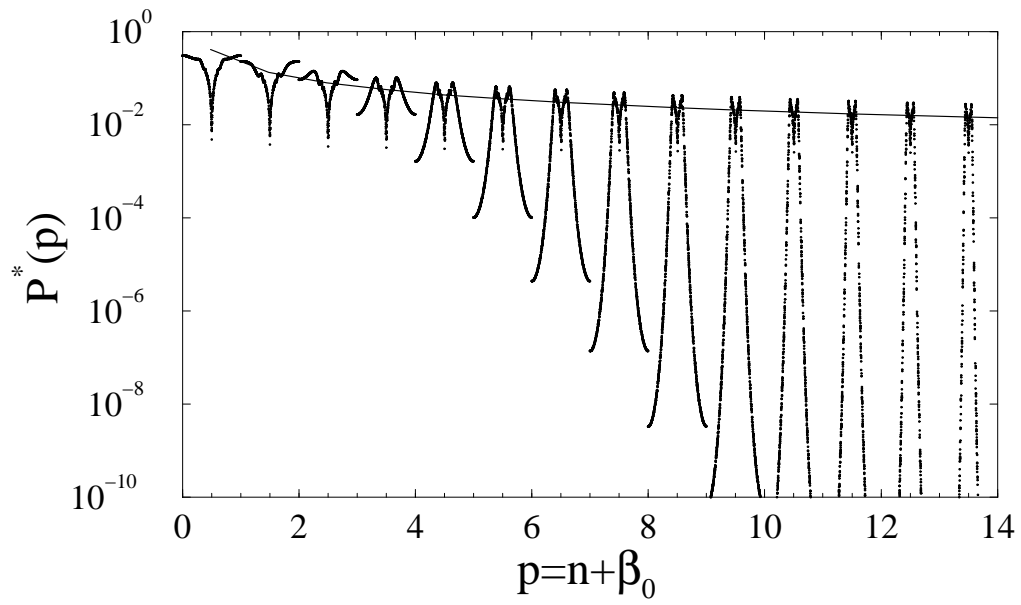


Figure 1: Time averaged stationary momentum distribution $P^*(p)$ for a uniform distribution of initial momentum $p_0 = \beta_0$ in $[0, 1)$, obtained by plotting (17) vs. $p = n + \beta_0$. The solid line drawn through the peak tops corresponds to a decay $\propto 1/n$.

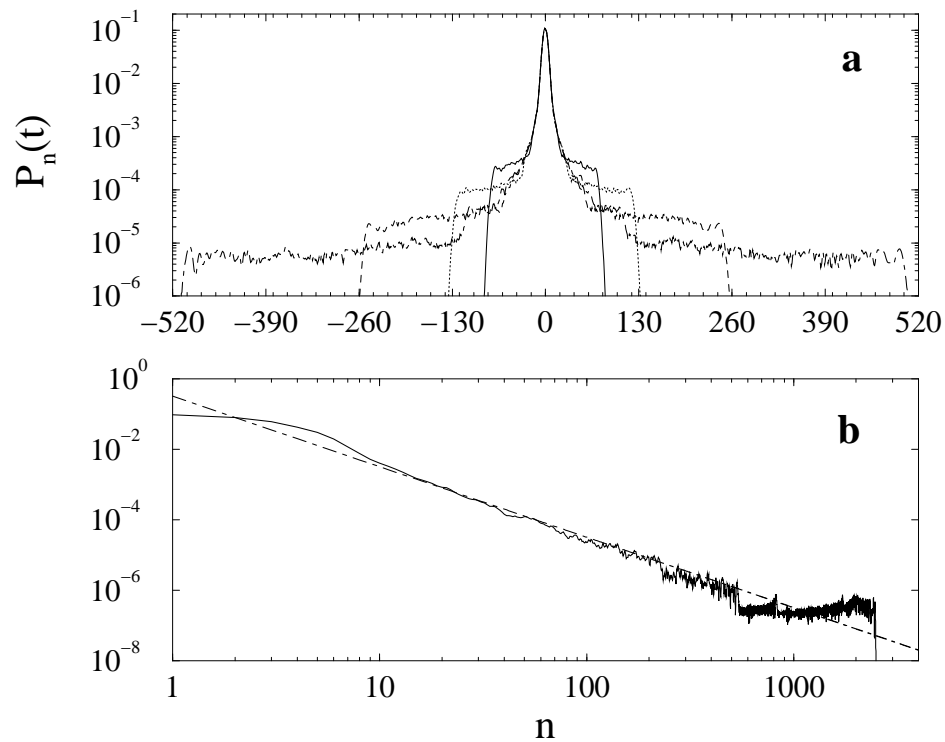


Figure 2: Evolution of coarse-grained momentum distributions (18) at resonance $\tau = 2\pi$, $k = 0.8\pi$ for an ensemble of 10^4 atoms, without decoherence. The initial momentum distribution is centred Gaussian, with rms deviation $\sigma \simeq 2.7$. (a): distributions for $t = 30$ (solid lines), $t = 50$ (dotted), $t = 100$ (dashed), $t = 200$ (dashed-dotted). (b): doubly logarithmic plot of the distribution at $t = 1000$ (solid line), compared to the asymptotic formula $4k/(\pi^3 n^2)$ (dashed-dotted line) (22). No cut-offs are used, so the distributions characterize the ideal behaviour of an ensemble of δ -kicked particles.

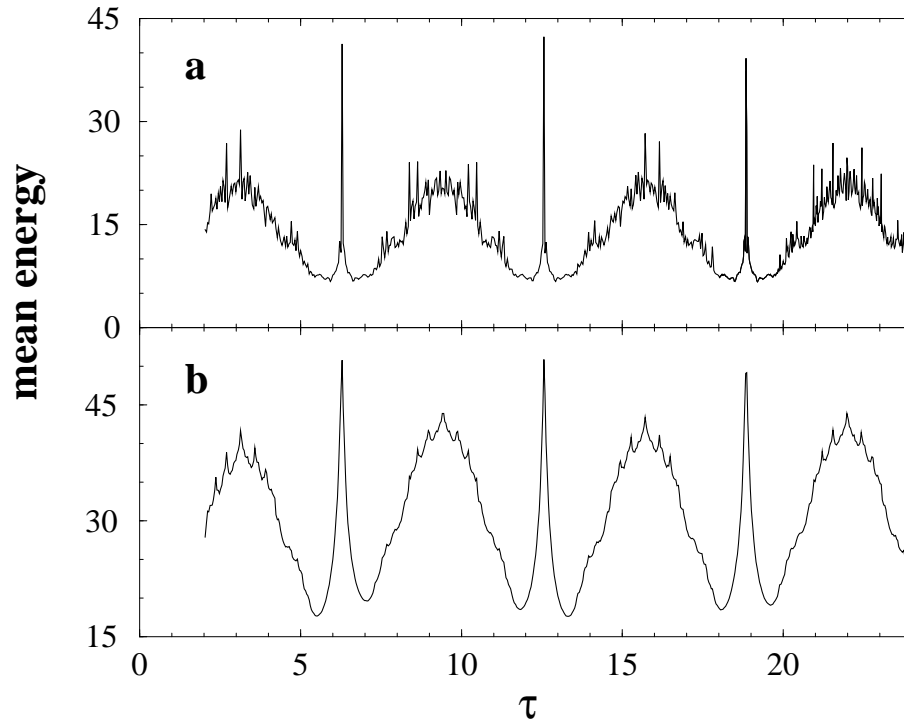


Figure 3: Mean energy after $t = 30$ kicks, vs. the kicking period τ , for an ensemble of 10^5 δ -kicked atoms, without momentum cut-offs, with the same initial distribution as in Fig. 2 and $k = 0.8\pi$. (a) no decoherence, (b) added spontaneous emission with rate $p_{\text{SE}} = 0.2$. Step-size in τ : $\delta\tau \simeq 0.03$, avoiding simple rational numbers; same results were obtained for a high-resolution random grid in the kicking period τ .

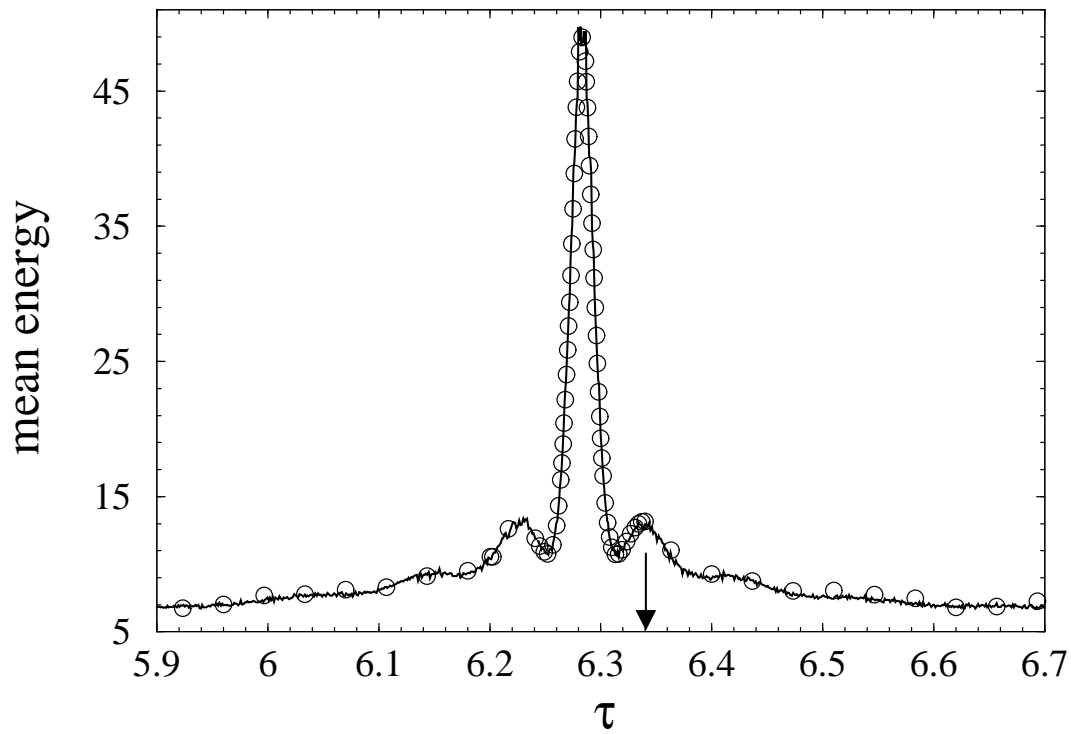


Figure 4: Magnification of Fig. 3(a) near the resonance $\tau = 2\pi$. Quantum data taken from Fig. 3(a) (circles) are compared with the mean energies of an ensemble of 10^6 ϵ -classical atoms (solid line) with the same initial momentum distribution, evolving under the ϵ -classical dynamics (27). The value of τ corresponding to the small peak on the right of the resonant spike is marked by an arrow for reference to Fig. 5.

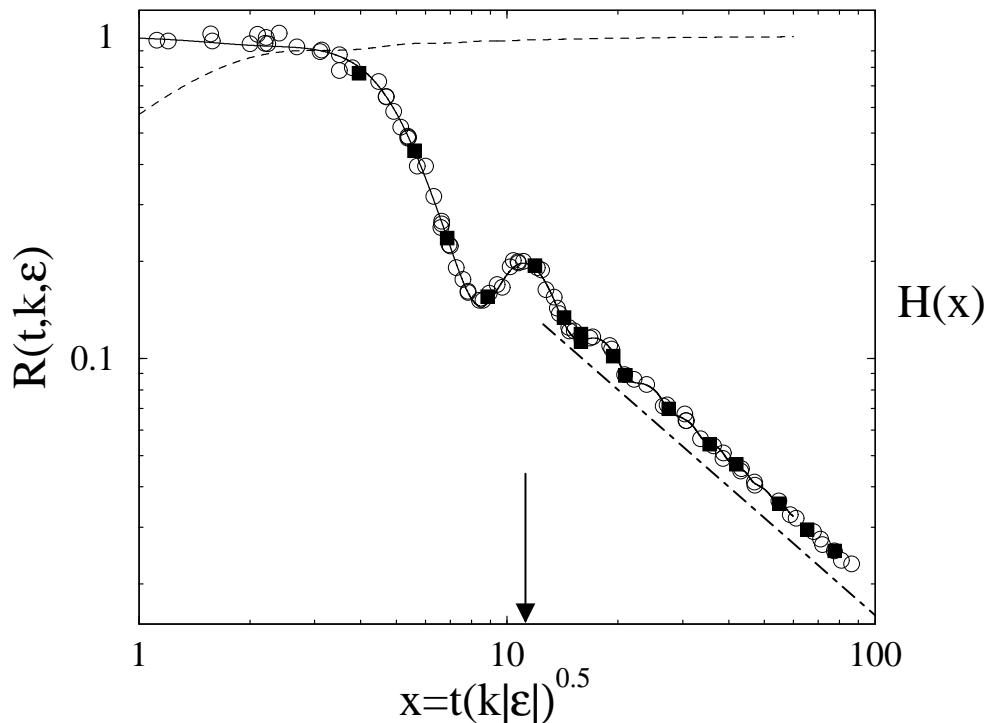


Figure 5: Demonstrating the scaling (36) of the resonant peak, in a right neighbourhood of $\tau = 2\pi$. Open circles correspond to different values of the parameters ϵ, k, t , randomly generated in the ranges $1 < t < 200$, $0.001 < \epsilon < 0.1$, $0.1 < k < 50$ with the constraint $0.01 < k\epsilon < 0.2$. In each case an ensemble of 2×10^6 ϵ -classical rotors was used to numerically compute the scaled energy $R(t, k, \epsilon)$ (36), with a uniform distribution of initial momenta in $[0, 1]$ and a uniform distribution of initial θ in $[0, 2\pi)$. Full squares present quantum data for $k = 0.8\pi$, $t = 50$ and $t = 200$. The solid line through the data is the scaling function $H(x)$ of (36) obtained by direct numerical computation of the functions $\Phi_0(x)$ and $G(x)$. The dashed line represents the function $\Phi_0(x)$; the dashed-dotted line has slope -1 and emphasizes the x^{-1} decay described in the text. The arrow marks the value of the scaled detuning x which corresponds to the arrow in Fig. 4.

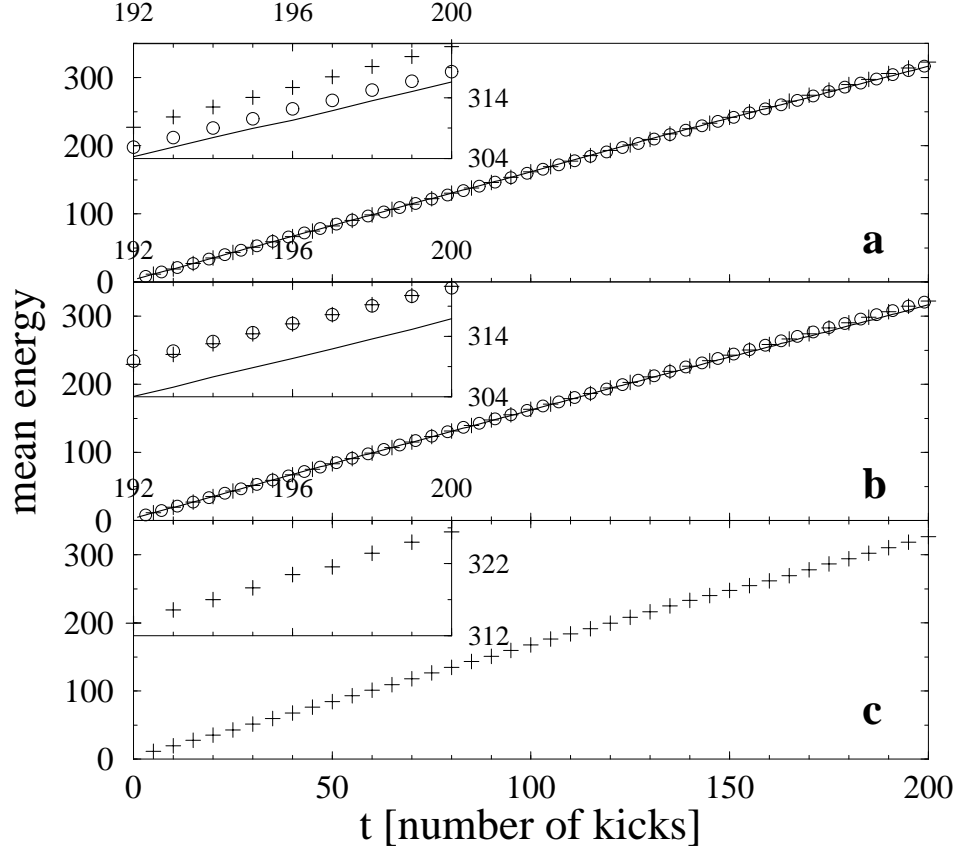


Figure 6: Average energy vs. time t at exact resonance $\tau = 2\pi$ for the same ensemble of atoms as in Fig. 2, for $k = 0.8\pi$, in the presence of SE events simulated in different ways as described in the text: (a) a random number of SEs occur immediately after kicks, each causing a momentum change δp uniformly distributed in $[-1/2, 1/2]$ (type (I) simulation). (b) SE times are Poisson-distributed in a window $\tau_{\text{SE}} = 0.067\tau$, with free evolution in-between them; δp is distributed as in (a). (c) SE times as in (a), but δp has the parabolic distribution (74) with $k_L/2k_T \simeq 0.476$. Rates of spontaneous emission $p_{\text{SE}} = 0.05$ (solid), $p_{\text{SE}} = 0.1$ (circles), $p_{\text{SE}} = 0.2$ (plusses). The theoretical prediction (see text) for the coefficient of linear growth D_{dec} is approximately 1.59, whereas the data lead to $D_{\text{dec}} \approx 1.58 - 1.60$ except in (b) for $p_{\text{SE}} = 0.05$ where it takes the value 1.55 (strong fluctuations). The insets zoom into the region close to $t = 200$. No momentum cutoffs are used.

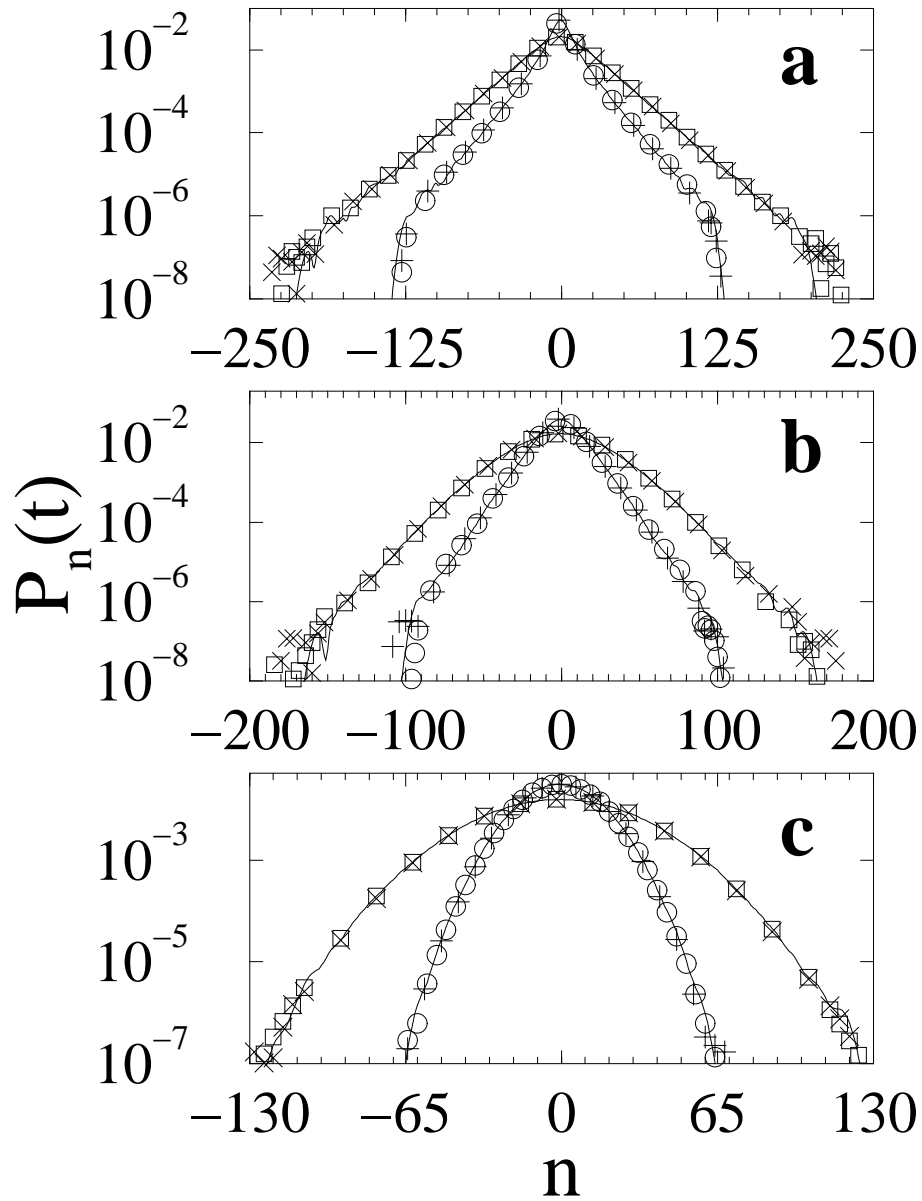


Figure 7: Evolution in time of coarse-grained momentum distributions for the same initial ensemble as in Fig. 2, and for $k = 0.8$, in the presence of SE. (a) $p_{\text{SE}} = 0.1$, (b) $p_{\text{SE}} = 0.2$, (c) $p_{\text{SE}} = 0.8$, for $t = 50$ and $t = 200$. The SE events are simulated in different ways. Solid lines were computed like in (a) in the previous figure; circles and squares, like in (b); plusses and crosses, like in (c) there.

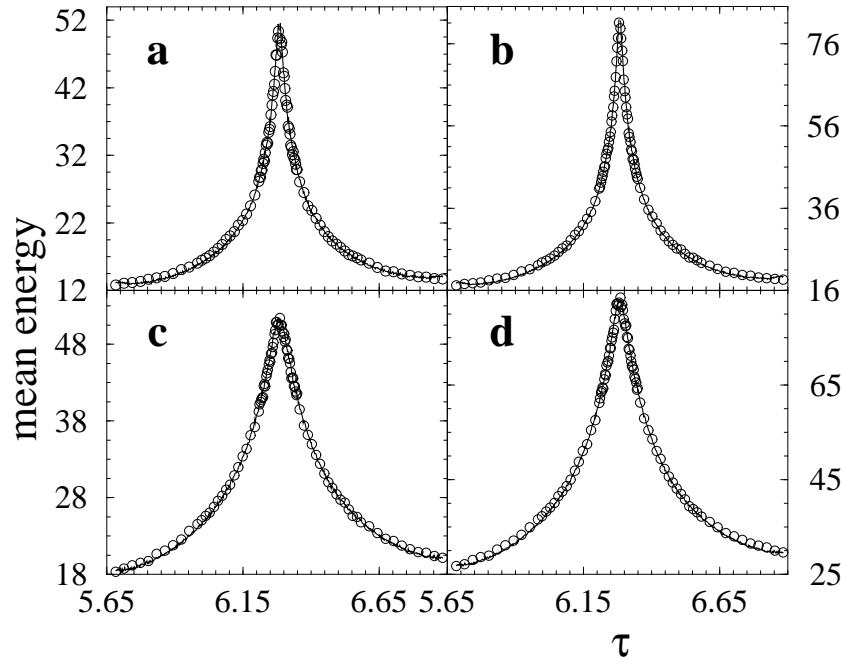


Figure 8: Analogue of Fig. 4, with the same initial ensemble, for $k = 0.8\pi$, in the presence of SE. Results of full quantum calculations (circles) and of ϵ -classical ones (solid lines) in the presence of SE are compared near the resonance $\tau = 2\pi$, for different times and different rates of SE: (a) $p_{SE} = 0.1, t = 30$, (b) $p_{SE} = 0.1, t = 50$, (c) $p_{SE} = 0.2, t = 30$, and (d) $p_{SE} = 0.2, t = 50$. The quantum simulation was type (I), while the ϵ -classical simulations used the map (76).

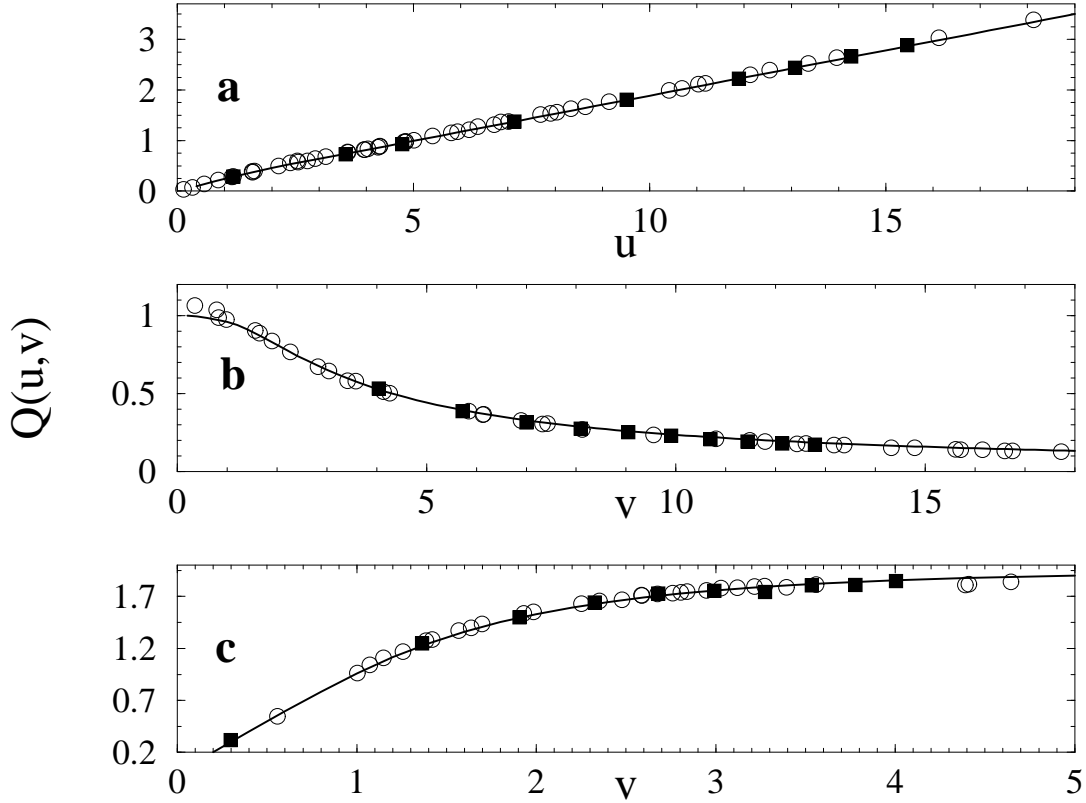


Figure 9: Demonstrating the scaling law (79) in a right neighbourhood of $\tau = 2\pi$. In (a), (b) the quantity on the lhs of eq. (80) is plotted vs. one of the parameters $u = t/t_c$ or $v = t_c/t_{res}$ while keeping the other fixed: (a) $v = 2$, (b) $u = 4$. In (c) the ratio $u/v = 4$ is fixed. Open symbols correspond to different values of the parameters t, t_c, k, ϵ , randomly generated in the ranges $1 < t < 200$, $5 < t_c < 60$, $0.001 < \epsilon < 0.1$, $0.1 < k < 20$, with the constraints $0.001 < k\epsilon < 0.2$ and $t_c\sqrt{k\epsilon} = 2$ in (a), $t/t_c = 4$ in (b), $t = 4t_c^2\sqrt{k\epsilon}$ in (c). In each case an ensemble of 2×10^6 ϵ -classical rotors was used, with a uniform distribution of initial momenta in $[0, 1]$ and a uniform distribution of initial θ in $[0, 2\pi)$. The random momentum shifts at each step of the ϵ -classical evolution (76) were generated from the uniform distribution in $[-1/2, 1/2]$. Full squares represent quantum data for $k = 0.8\pi$, and $\epsilon = 0.01$ in (a), $\epsilon = 0.05$ in (c), and $t = 50$ and $t = 100$ in (b). The solid lines correspond to the theoretical formula (81).

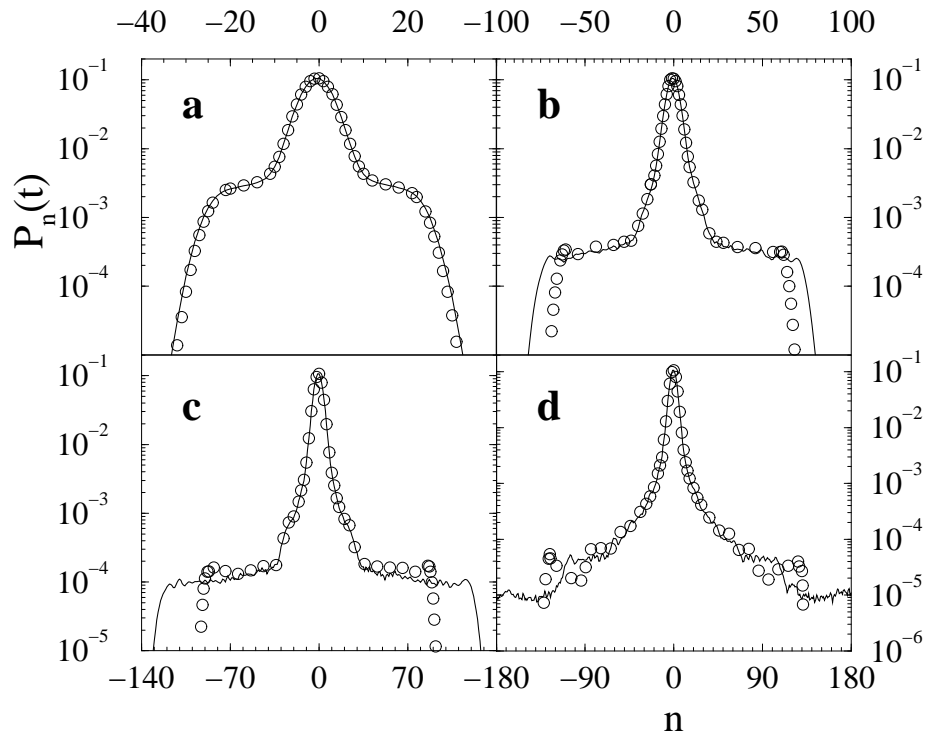


Figure 10: Coarse-grained momentum distributions for the same initial ensemble as in Fig. 2 and without SE, for $k = 0.8\pi$ and $\tau = 2\pi$. The ideal case of δ -kicks (solid line) is compared to the case of rectangular pulses (open circles). Times are $t = 10$ (a), 30 (b), 50 (c), 200 (d).

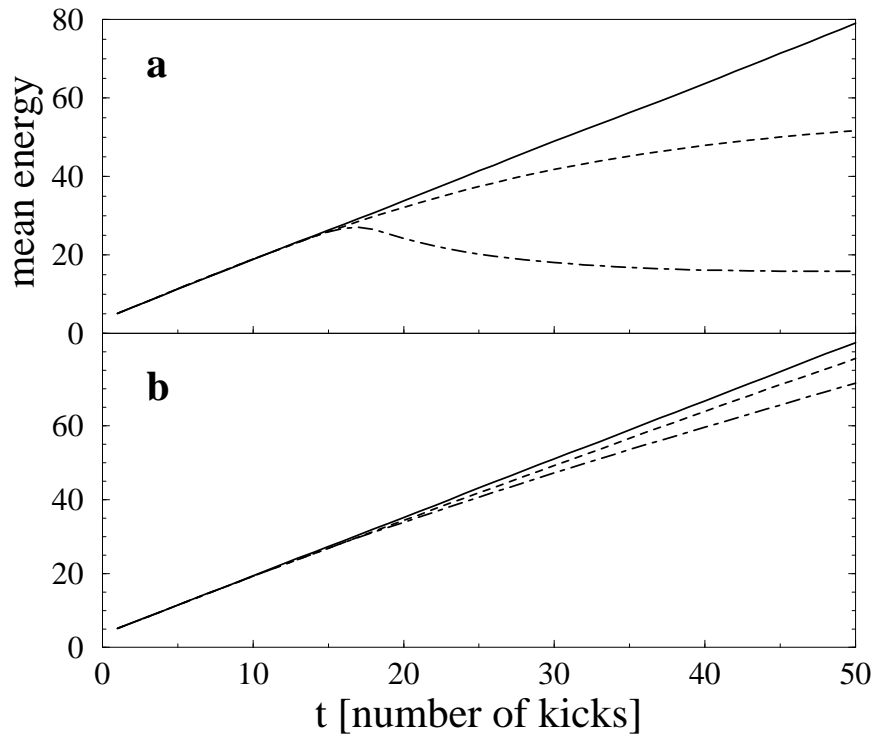


Figure 11: Effect of finite pulse width and of momentum cutoff on the growth of the mean energy for the same initial ensemble as in Figs. 2 and 10, for $k = 0.8\pi$ and $\tau = 2\pi$, without SE (a) and with $p_{SE} = 0.2$ (b). Solid lines are for the ideal δ -kicks and no momentum cutoff; dashed lines for rectangular pulses, no cutoff; dashed-dotted lines for rectangular pulses and momentum cutoff at $n_{cut} = 40$. In (a) the energy is significantly depressed by the cutoff after $t > 20$, not so in (b).

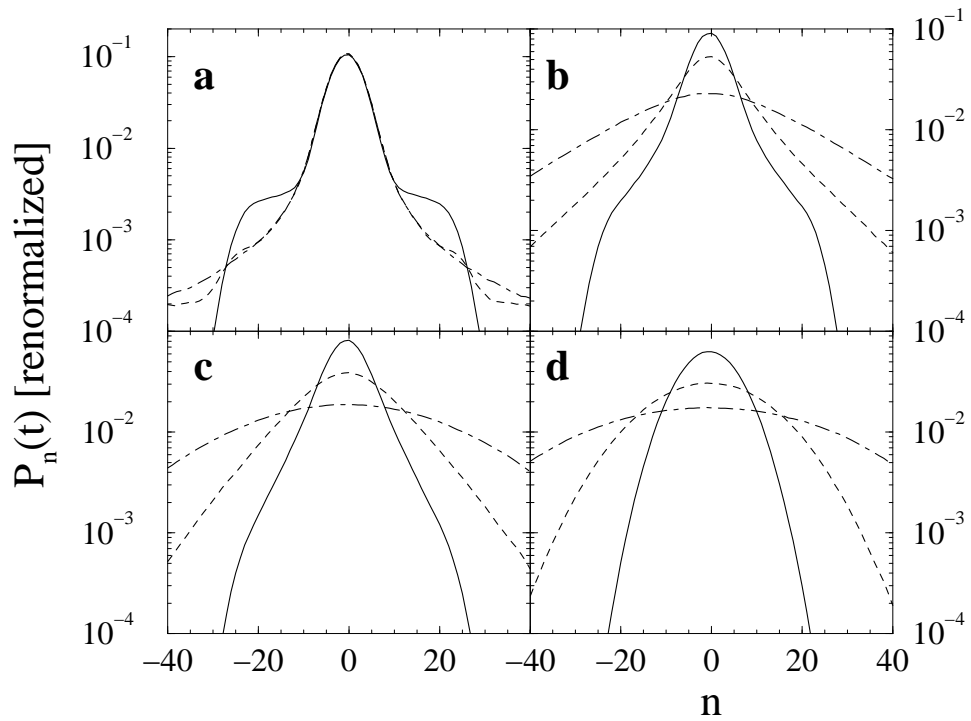


Figure 12: Evolution of coarse-grained momentum distribution for the same ensemble as in Figs. 2 and 10, for $\tau = 2\pi$ and $k = 0.8\pi$, with rectangular pulses and momentum cutoff at $n_{cut} = 40$. (a) $p_{SE} = 0$, (b) $p_{SE} = 0.1$, (c) $p_{SE} = 0.2$, (d) $p_{SE} = 0.8$, after $t = 10$ (solid lines), $t = 50$ (dashed), $t = 200$ (dashed-dotted)

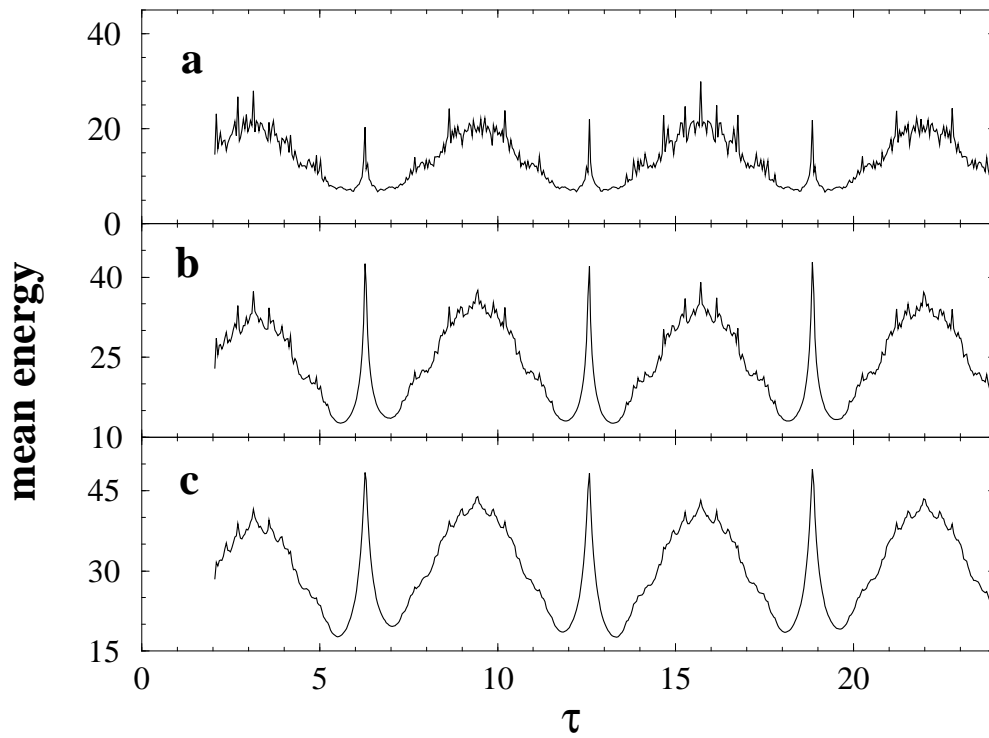


Figure 13: Mean energy as a function of the kicking period τ for the same ensemble of SE and the same initial distribution of atoms as in Fig. 3, after 30 kicks for $k = 0.8\pi$. (a) no decoherence $p_{\text{SE}} = 0$, (b) $p_{\text{SE}} = 0.1$, (c) $p_{\text{SE}} = 0.2$. The width of the rectangular pulse is $\tau_p = 0.047$ and $n_{\text{cut}} = 40$, as in the experiments [32, 33]. The shown range of τ corresponds in laboratory units to $21.2 \dots 254.7 \mu\text{sec}$.